

ACCRETION OF INTERPLANETARY DUST PARTICLES BY THE EARTH

By

STEPHEN JOHN KORTENKAMP

A DISSERTATION PRESENTED TO THE GRADUATE SCHOOL
OF THE UNIVERSITY OF FLORIDA IN PARTIAL FULFILLMENT
OF THE REQUIREMENTS FOR THE DEGREE OF
DOCTOR OF PHILOSOPHY

UNIVERSITY OF FLORIDA

1996

To Mom and Dad.

ACKNOWLEDGMENTS

I thank my advisor Stan Dermott for his help over the last few years and for instilling in me a sense of awe for anything published in *Nature*. I also thank Humberto Campins for his support in the first year of my stay at the University of Florida. Thanks also go to the other members of my committee, Bo Gustafson, Henry Kandrup and Paul Mueller. Finally, I thank my parents for raising me the way they did.

TABLE OF CONTENTS

	<u>page</u>
ACKNOWLEDGMENTS	iii
LIST OF TABLES	vi
LIST OF FIGURES	vii
ABSTRACT	xix
 CHAPTERS	
1 INTRODUCTION	1
2 DUST IN THE ZODIACAL CLOUD	4
3 THE MECHANICS OF ACCRETION	15
Average Spatial Density	15
Relative Encounter Velocity	24
Gravitational Cross-Section	25
Capture Rate	28
4 THE ORIGIN OF IDPS	30
Initial Parent Body Population	31
Generation and Evolution of Dust Particle Orbits	32
Capture Rates	36
Contribution to the IDPs	37
5 VARIATIONS IN THE RATE OF ACCRETION	62
Initial Conditions	63
Generation and Evolution of Dust Particle Orbits	64
Variable Capture Rates	68
Comparison With Other Records	73
6 SUMMARY	95
Conclusions and Discussion	95
Future Work – The Role of Resonance	97

BIBLIOGRAPHY	104
BIOGRAPHICAL SKETCH	108

LIST OF TABLES

<u>Table</u>	<u>page</u>
2-1: The area of dust contributed from each family is the same in both the 2.°5 and the 3.°5 models. However, in the 3.5° model material is distributed between the asteroid belt and the Sun whereas in the 2.°5 model the material is confined to the asteroid belt.	14
4-1: Normalized average capture rates.	39
5-1: Proper elements and dispersions for 1 micron diameter particles at 1AU.	67
5-2: Proper elements and dispersions for 10 micron diameter particles at 1AU.	68

LIST OF FIGURES

<u>Figure</u>		<u>page</u>
2-1:	<p>IRAS observation of the zodiacal cloud in the $25\mu\text{m}$ infrared waveband (solid upper curve). This observation was made at 90° solar elongation angle (the angle between the telescope pointing direction and the Earth-Sun line) in the direction leading the Earth in its orbit when the planet was at an ecliptic longitude of 293°. The dust bands can be seen as projecting "shoulders" near $\pm 10^\circ$ and 0° latitude. The structure around 60° latitude is due to dust in the plane of the Galaxy. By applying a Fourier filter to the IRAS observation a smooth background profile (underlying dashed curve) is separated from a high frequency dust band profile (solid lower curve). This filtered high frequency dust band profile is merely a residual representing the "tip of the iceberg" in terms of the dust band material in the zodiacal cloud.</p>	10
2-2:	<p>Filtered IRAS dust band profiles (solid lines) for eight different longitudes of the Earth (λ_\oplus). All profiles were made at 90° solar elongation angle in the direction leading the Earth in its orbit. Model dust bands were constructed using particles from the Themis and Koronis families for the central band-pair and the Eos family for the 10° band-pair. A dispersion of $2.^\circ 5$ was imposed on the proper inclination of the Eos material in this model. All of the material in this model was confined to the asteroid belt. Eight simulated profiles (dashed lines) which mimic the IRAS $25\mu\text{m}$ infrared waveband were made through these model dust bands at the same longitudes and elongation angle as the IRAS profiles. These simulated profiles were filtered in a fashion identical to that used to generate the IRAS profiles. Dashed vertical lines are placed at $\pm 10^\circ$ for reference. All profiles have an amplitude of around 2 MJy/Sr but are staggered in the figure for convenience.</p>	11
2-3:	<p>Same as in Figure 2-2 except these filtered model dust band profiles (dashed lines) are for the $3.^\circ 5$ model in which the Eos material is distributed from the asteroid belt to the Sun.</p>	12

2-4:	Unfiltered IRAS observation shown in Figure 2-1. The lower and middle curves are simulated unfiltered profiles mimicking the IRAS $25\mu\text{m}$ infrared waveband taken through two different dust band models. Each of these dust band models was constructed using particles from only the three asteroid families Eos, Themis and Koronis. The model profile labeled 2. $^{\circ}5$ uses Eos particles having a 2. $^{\circ}5$ dispersion in proper inclination and confines all particles to the asteroid belt. The model profile labeled 3. $^{\circ}5$ is constructed using Eos particles with a 3. $^{\circ}5$ dispersion in proper inclination and by allowing the Eos material to stretch from the asteroid belt to the inner Solar System. The difference in the peak intensity between a given model profile and the IRAS profile indicates the dust band contribution to the entire zodiacal cloud, listed in Table 2-1.	13
3-1:	Demonstration of the concept of forced and proper orbital elements. . . .	16
3-2:	Osculating orbital elements for 357 members of the Themis asteroid family.	17
3-3:	Radial dependence of the spatial density.	19
3-4:	Latitude dependence of the spatial density and volume of latitude element of spherical shell.	22
3-5:	Latitude (left) and radial (right) average spatial density distributions. An orbit with $a = 1$, $e = 0.05$ and $I = 1.^{\circ}5$ was used, the Sun is at the origin off the figure to the left.	23
3-6:	Velocity vector relationship for determining encounter velocity.	24
3-7:	Hyperbolic deflection of a particle encountering the Earth.	26
4-1:	Distribution of osculating inclination verses semi-major axis for 118 short period Jupiter family comets.	41
4-2:	Distribution of osculating eccentricity verses semi-major axis for 118 short period Jupiter family comets. The dashed line marks the extreme limit of the Jupiter-crossing regime, using a semi-major axis and eccentricity of $a = 5.203$, $e = 0.062$ for Jovian orbit. These give a perihelion of $q = 4.88$ AU, which we further reduce by subtracting the sphere of action of the planet, $D_a \simeq 0.365$ AU.	42

- 4-3: Histograms showing the inclination and eccentricity distributions of the comets plotted in Figures 4-1 and 4-2. 43
- 4-4: Distribution of proper inclination verses semi-major axis for all asteroids with absolute magnitude $H < 11$ (1053 asteroids). This plot is shown on the same scale as Figure 4-1 (with a shift of 1AU in semi-major axis) and shows that the Jupiter family of comets span the same range of inclination as the asteroids in the main belt. The asteroid family Eos is the cluster at approximately 3AU and 10° inclination. The Koronis and Themis families are the low inclination clusters to the left and right of 3AU, respectively. Notice that the Eos and Themis families have a higher dispersion in proper inclination than the Koronis family. 44
- 4-5: The top plot is a histogram of the all the asteroids shown in Figure 4-4. The middle plot shows only those asteroids of Figure 4-4 that are associated with families. The bottom plot is all the remaining background asteroids that are not associated with families. The families Themis and Koronis appear together at the feature inside of 3° proper inclination, Eos is at 10° and the next largest family Maria is at 15° . Several small families are also visible. From this plot we see that a large majority of the low inclination asteroids belong to the Themis and Koronis families and that more than half of the asteroids at 10° belong to the Eos family. . . 45
- 4-6: Distribution of proper eccentricity verses semi-major axis for all asteroids with absolute magnitude $H < 11$ (1053 asteroids). This plot, which is shown on the same scale as Figure 4-2 (with a shift of 1AU in semi-major axis), reveals the primary difference between the Jupiter family cometary population and the asteroidal population. The comets have much higher eccentricities. The asteroid families Eos and Koronis are apparent at 3AU, and just inside of 3AU respectively. The Themis family is slightly more difficult to discern here than in Figure 4-4, lying between 3.1 and 3.2 AU at about 0.15 in proper eccentricity. 46
- 4-7: The top plot is a histogram of the all the asteroids shown in Figure 4-6. The middle plot shows only those asteroids of Figure 4-6 that are associated with families. The bottom plot is all the remaining background asteroids that are not associated with families. 47
- 4-8: Distribution of osculating inclination verses semi-major axis for Earth-crossing orbits of cometary dust particles. The obvious tracking is due to the continuing evolution of particles from a single comet. 48

- 4-9: Distribution of osculating eccentricity verses semi-major axis for Earth-crossing orbits of cometary dust particles. The obvious tracking is due to the continuing evolution of particles from a single comet. 49
- 4-10: Smoothed distribution of osculating inclination verses semi-major axis for Earth-crossing orbits of cometary dust particles. We use the mean and dispersion of the orbital elements shown in Figure 4-8 to generate a random gaussian distribution of Earth-crossing cometary orbits. 50
- 4-11: Smoothed distribution of osculating eccentricity verses semi-major axis for Earth-crossing orbits of cometary dust particles. We use the mean and dispersion of the orbital elements shown in Figure 4-9 to generate a random gaussian distribution of Earth-crossing cometary orbits. 51
- 4-12: Distribution of proper inclination verses semi-major axis for Earth-crossing orbits of non-family asteroidal particles. This plot is shown on the same scale as Figure 4-10 and shows that the Earth-crossing cometary population spans the same range of inclination as the Earth-crossing asteroidal population. 52
- 4-13: Distribution of proper eccentricity verses semi-major axis for Earth-crossing orbits of non-family asteroidal particles. This plot, which is shown on the same scale as Figure 4-11 reveals the primary difference between the Earth-crossing cometary population and the Earth-crossing asteroidal population. The cometary orbits have much higher eccentricities. As we will see, this leads to substantially higher geocentric encounter velocities for cometary particles than for asteroidal particles. . . 53
- 4-14: The orbital evolution of a wave of 10 micron diameter dust particles from the Eos family as their orbits decay from the asteroid family at 3AU into the inner Solar System. The middle plot tracks the evolution of the proper inclination and dispersion in proper inclination of the particles as their semi-major axes decay due to P-R drag. The displacement from the origin of the distributions in the upper two plots is due to the forced inclination, which is shown in the lower plot. 54

- 4-15: The orbital evolution of a wave of 10 micron diameter dust particles from the Eos family as their orbits decay from the asteroid family at 3AU into the inner Solar System. The middle plot tracks the evolution of the proper eccentricity and dispersion in proper eccentricity of the particles as their semi-major axes decay due to P-R drag. P-R drag also acts to reduce the proper eccentricity of the particles as their orbits decay towards the Sun. The displacement from the origin of the distributions in the upper two plots is due to the forced eccentricity, which is shown in the lower plot. At 1AU the distribution is nearly centered on the origin, indicating a very small forced eccentricity. . . . 55
- 4-16: The orbital evolution of a wave of 10 micron diameter dust particles from the Themis family as their orbits decay from the asteroid family at 3.1 AU into the inner Solar System. The middle plot tracks the evolution of the proper inclination and dispersion in proper inclination of the particles as their semi-major axes decay due to P-R drag. The displacement from the origin of the distributions in the upper two plots is due to the forced inclination, which is shown in the lower plot. . . . 56
- 4-17: The orbital evolution of a wave of 10 micron diameter dust particles from the Themis family as their orbits decay from the asteroid family at 3.1 AU into the inner Solar System. The middle plot tracks the evolution of the proper eccentricity and dispersion in proper eccentricity of the particles as their semi-major axes decay due to P-R drag. P-R drag also acts to reduce the proper eccentricity of the particles as their orbits decay towards the Sun. The displacement from the origin of the distributions in the upper two plots is due to the forced eccentricity, which is shown in the lower plot. At 1AU the distribution is nearly centered on the origin, indicating a very small forced eccentricity. . . . 57
- 4-18: The orbital evolution of a wave of 10 micron diameter dust particles from the Koronis family as their orbits decay from the asteroid family at 2.9 AU into the inner Solar System. The middle plot tracks the evolution of the proper inclination and dispersion in proper inclination of the particles as their semi-major axes decay due to P-R drag. The displacement from the origin of the distributions in the upper two plots is due to the forced inclination, which is shown in the lower plot. . . . 58

- 4-19: The orbital evolution of a wave of 10 micron diameter dust particles from the Koronis family as their orbits decay from the asteroid family at 2.9 AU into the inner Solar System. The middle plot tracks the evolution of the proper eccentricity and dispersion in proper eccentricity of the particles as their semi-major axes decay due to P-R drag. P-R drag also acts to reduce the proper eccentricity of the particles as their orbits decay towards the Sun. The displacement from the origin of the distributions in the upper two plots is due to the forced eccentricity, which is shown in the lower plot. At 1AU the distribution is nearly centered on the origin, indicating a very small forced eccentricity. 59
- 4-20: Capture rates for dust particles on the Earth-crossing orbits shown in Figures 4-10 through 4-19 are plotted against the geocentric encounter velocity of the particles. This is the velocity of the particles prior to being accelerated by the Earth's gravitational field. The average capture rate for non-family asteroidal particles is designated by the large crossed circle at 150 Gyr^{-1} and 6 km s^{-1} . Cometary capture rates are the crossed points, Eos rates the open circles and Themis and Koronis rates the filled circles. 60
- 4-21: Percentages of IDPs in the atmosphere are determined by combining the data of Figure 4-20 with the information shown in Table 2-1. 61
- 5-1: Comparison of the inclination and longitude of ascending node of the Earth's orbit determined by backwards integration of the Solar System with the RADAU integrator (dashed lines – Mercury and Pluto excluded) and from Quinn et al. (1991; solid lines – all planets included). These orbital elements are with respect to the J2000 ecliptic and mean equinox. Quinn et al. report that the largest error in their calculated orbital elements of the Earth is not greater than 4 parts in 10^6 after 3 million years of integration. After less than 100,000 years of integration there are noticeable differences between the two curves. . . . 75
- 5-2: Comparison of the inclination and longitude of ascending node of Jupiter's orbit determined by backwards integration of the Solar System with the RADAU integrator (dashed lines – Mercury and Pluto excluded) and from Quinn et al. (solid lines – all planets included). These orbital elements are with respect to the J2000 ecliptic and mean equinox. The orbits of the more massive Jovian planets are more stable than the orbit of the Earth in the RADAU integrator. 76

- 5-3: Comparison of the forced inclination and forced longitude of ascending node of the asteroid families Eos, Themis and Koronis with the inclination and longitude of ascending node of Jupiter's orbit. The orbital elements of the members of these three asteroid families were determined by backwards integration of the Solar System with the RADAU integrator (Mercury and Pluto excluded). These orbital elements are with respect to the J2000 ecliptic and mean equinox. The forced plane of symmetry of these three asteroid families is essentially locked onto the orbit of Jupiter. 77
- 5-4: Waves of 249 particles with diameters of 1 and 10 microns were released from the asteroid family Eos every 20,000 years. These waves became Earth-crossing at the time indicated on the horizontal axis. At this point the mutual inclination between the orbit of the Earth and the forced plane of symmetry of each wave is calculated (1 micron – filled circle; 10 micron – open circle). The solid line is the mutual inclination between the orbits of the Earth and Jupiter from Quinn et al. Since the forced plane of symmetry of the asteroid families is locked onto the orbit of Jupiter (see Figure 5-3) this solid line represents the initial forced plane of symmetry of the waves of dust particles in the asteroid belt. This plot shows that the orbits of the 1 micron diameter particles decay into the inner Solar System so fast that they essentially retain their initial forced plane of symmetry. The 10 micron diameter particles evolve more slowly and therefore are more susceptible to perturbations which change their forced plane of symmetry. 78
- 5-5: The orbital evolution of a wave of 1 micron diameter dust particles from the Eos family as their orbits decay from the asteroid family at 3AU into the inner Solar System. The middle plot tracks the evolution of the proper inclination and dispersion in proper inclination of the particles as their semi-major axes decay due to P-R drag. The displacement from the origin of the distributions in the upper two plots is due to the forced inclination, which is shown in the lower plot. . . . 79

- 5-6: The orbital evolution of a wave of 1 micron diameter dust particles from the Eos family as their orbits decay from the asteroid family at 3 AU into the inner Solar System. The middle plot tracks the evolution of the proper eccentricity and dispersion in proper eccentricity of the particles as their semi-major axes decay due to P-R drag. P-R drag also acts to reduce the proper eccentricity of the particles as their orbits decay towards the Sun. The displacement from the origin of the distributions in the upper two plots is due to the forced eccentricity, which is shown in the lower plot. At 1 AU the distribution is nearly centered on the origin, indicating a very small forced eccentricity. . . . 80
- 5-7: The orbital evolution of a wave of 1 micron diameter dust particles from the Themis family as their orbits decay from the asteroid family at 3.1 AU into the inner Solar System. The middle plot tracks the evolution of the proper inclination and dispersion in proper inclination of the particles as their semi-major axes decay due to P-R drag. The displacement from the origin of the distributions in the upper two plots is due to the forced inclination, which is shown in the lower plot. . . . 81
- 5-8: The orbital evolution of a wave of 1 micron diameter dust particles from the Themis family as their orbits decay from the asteroid family at 3.1 AU into the inner Solar System. The middle plot tracks the evolution of the proper eccentricity and dispersion in proper eccentricity of the particles as their semi-major axes decay due to P-R drag. P-R drag also acts to reduce the proper eccentricity of the particles as their orbits decay towards the Sun. The displacement from the origin of the distributions in the upper two plots is due to the forced eccentricity, which is shown in the lower plot. At 1 AU the distribution is nearly centered on the origin, indicating a very small forced eccentricity. . . . 82
- 5-9: The orbital evolution of a wave of 1 micron diameter dust particles from the Koronis family as their orbits decay from the asteroid family at 2.9 AU into the inner Solar System. The middle plot tracks the evolution of the proper inclination and dispersion in proper inclination of the particles as their semi-major axes decay due to P-R drag. The displacement from the origin of the distributions in the upper two plots is due to the forced inclination, which is shown in the lower plot. . . . 83

5-10: The orbital evolution of a wave of 1 micron diameter dust particles from the Koronis family as their orbits decay from the asteroid family at 2.9 AU into the inner Solar System. The middle plot tracks the evolution of the proper eccentricity and dispersion in proper eccentricity of the particles as their semi-major axes decay due to P-R drag. P-R drag also acts to reduce the proper eccentricity of the particles as their orbits decay towards the Sun. The displacement from the origin of the distributions in the upper two plots is due to the forced eccentricity, which is shown in the lower plot. At 1AU the distribution is nearly centered on the origin, indicating a very small forced eccentricity. . . . 84

5-11: Demonstration of the variation in the capture rate: (Top) Varying eccentricity of the Earth's orbit from Quinn et al.; (Middle) Sine wave variation in the mutual inclination between the orbit of the Earth and the forced plane of symmetry of a dust band at 1AU. The base line of the mutual inclination is $1.^\circ 4$; (Bottom) Variation in the normalized capture rate for dust particles with proper elements and dispersions equal to those of Themis 1 micron diameter particles at 1AU (See Table 5-1). The proper inclination is indicated by the dashed line in the middle plot. The variation of the Earth's eccentricity reveals itself in the capture rate, which appears to have been lopped off at points where the eccentricity is increasing or decreasing. There is also a subtle 400,000 periodicity in the varying capture rate due to the eccentricity, this is superimposed over the 100,000 year periodicity due to the mutual inclination. 85

5-12: Demonstration of the annual motion of the Earth through an ideal dust band. The orbits in this idealized dust band have a proper inclination of $1.^\circ 5$ and no dispersion in proper inclination. Four different values of the mutual inclination (I_{\oplus}) between the orbit of the Earth and the forced plane of symmetry of the dust band are shown. When the mutual inclination is lower than the proper inclination of the dust band the Earth is embedded within the dust band throughout its entire orbit. However, when the mutual inclination is greater than the proper inclination of the dust band the Earth emerges from the dust band twice each year. The higher the mutual inclination is, the less time the Earth spends in the dust band each year. Also, the higher mutual inclination leads to greater geocentric encounter velocities of the dust particles when the Earth is in the dust band. 86

- 5-13: Variation in the capture rate of 1 micron diameter Themis particles: (Top) Varying eccentricity of the Earth's orbit from Quinn et al.; (Middle) Variation in the mutual inclination between the orbit of the Earth and the forced plane of symmetry of 1 micron diameter dust particles at 1AU; (Bottom) Variation in the normalized capture rate for dust particles with proper elements and dispersions equal to those of Themis 1 micron diameter particles at 1AU (See Table 5-1). The proper inclination is indicated by the dashed line in the middle plot. The capture rate of these small Themis dust particles drops dramatically when the Earth is not embedded within the dust band. 87
- 5-14: Variation in the capture rate of 1 micron diameter Koronis particles: (Top) Varying eccentricity of the Earth's orbit from Quinn et al.; (Middle) Variation in the mutual inclination between the orbit of the Earth and the forced plane of symmetry of 1 micron diameter dust particles at 1AU; (Bottom) Variation in the normalized capture rate for dust particles with proper elements and dispersions equal to those of Koronis 1 micron diameter particles at 1AU (See Table 5-1). The proper inclination is indicated by the dashed line in the middle plot. Because of the higher proper inclination the mutual inclination doesn't rise as far above the proper inclination and so the capture rate variations are not as dramatic as for the Themis particles. 88
- 5-15: Variation in the capture rate of 1 micron diameter Eos particles: (Top) Varying eccentricity of the Earth's orbit from Quinn et al.; (Middle) Variation in the mutual inclination between the orbit of the Earth and the forced plane of symmetry of 1 micron diameter dust particles at 1AU; (Bottom) Variation in the normalized capture rate for dust particles with proper elements and dispersions equal to those of Eos 1 micron diameter particles at 1AU (See Table 5-1). Only the variation due to the Earth's eccentricity is evident in the capture rates. 89
- 5-16: Variation in the capture rate of 10 micron diameter Themis and Koronis particles: (Top) Varying eccentricity of the Earth's orbit from Quinn et al.; (Middle) Variation in the mutual inclination between the orbit of the Earth and the forced plane of symmetry of 10 micron diameter dust particles at 1AU; (Bottom) Variation in the normalized capture rate for dust particles with proper elements and dispersions equal to those of Themis and Koronis 10 micron diameter particles at 1AU (See Table 5-2). The proper inclination is indicated by the dashed line in the middle plot. Because of the higher proper inclination and the higher dispersion the capture rates of these larger particles do not show the large variations associated with the smaller 1 micron diameter particles. . . . 90

- 5-17: Variation in the capture rate of 10 micron diameter Eos particles: (Top) Varying eccentricity of the Earth's orbit from Quinn et al.; (Middle) Variation in the mutual inclination between the orbit of the Earth and the forced plane of symmetry of 10 micron diameter dust particles at 1AU; (Bottom) Variation in the normalized capture rate for dust particles with proper elements and dispersions equal to those of Eos 10 micron diameter particles at 1AU (See Table 5-2). The effect of the varying mutual inclination is completely absent from the capture rate and only the variation due to the Earth's eccentricity remains. Since Eos particles have a proper inclination about equal to the mean for the asteroid belt we expect that any variation in the accretion of background asteroidal particles will follow the variations shown here. 91
- 5-18: Comparison of the capture rates for Themis and Koronis particles with the ^3He record for the period between 250,000 and 450,000 years ago: (Top) Capture rates (Gyr^{-1}) for particles of diameter 20 (open circles), 10 (solid circles) and 1 micron (high resolution line – Themis only); (Bottom) Variation in the flux of extraterrestrial ^3He ($10^{-12} \text{ cm}^3 \text{ STP cm}^{-2} \text{ kyr}^{-1}$) to the sea floor from Farley and Patterson (1995). Only the 1 micron diameter capture rate displays a variation with an amplitude and period comparable with that of the ^3He flux, however, the two curves are not in phase. 92
- 5-19: Comparison of the capture rates for Eos particles with the ^3He record for the period between 250,000 and 450,000 years ago: (Top) Capture rates (Gyr^{-1}) for particles of diameter 20 (open circles), 10 (solid circles) and 1 micron (high resolution line); (Bottom) Variation in the flux of extraterrestrial ^3He ($10^{-12} \text{ cm}^3 \text{ STP cm}^{-2} \text{ kyr}^{-1}$) to the sea floor from Farley and Patterson (1995). Note that only the 1 micron diameter capture rate displays a variation with an amplitude and period comparable with that of the ^3He flux, however, the two curves are not in phase. . . . 93
- 5-20: Comparison of the capture rates for 1 micron diameter Themis particles with the climate record for the last 1.2 million years: (Top) Normalized capture rate for 1 micron diameter Themis particles (dashed line) and the filtered climate record (solid line, $\delta^{18}\text{O}$ – oxygen isotope ratios in deep-sea sediments) for the last 1.2 million years. The climate record is shown after removal of the well understood shorter period Milankovitch frequencies (Imbrie et al. 1993); (Middle) Power spectrum of the capture rate for 0–600 ka (ka – 10^3 years ago) and 600–1200 ka; (Bottom) Power spectrum of filtered climate record for 0–600 ka and 600–1200 ka. . . . 94

- 6-1: Stochastic variations in the cross-sectional area of debris down to 1mm from the breakup of a large asteroid and its continued collisional evolution. The area associated with the fragments is an indicator of the dust production rate of the debris. The smaller spikes are due to the continuing breakup of smaller 10-40 km diameter bodies. This figure is from Durda et al. (1992). 99
- 6-2: Incremental mass of particles accreted by the Earth annually as a function of particle mass and diameter (number in each bin times the average mass for each bin). The bold line is calculated from the polynomial derived by Love and Brownlee (1993) from the cratering record on LDEF. The individual points with errors are calculated from the incremental crater density counts provided by S. Love (personal communication). As expected, the mass accretion is dominated by the larger particles. . . . 100
- 6-3: Incremental cross-sectional area of particles accreted by the Earth annually as a function of particle mass and diameter (number in each bin times the average cross-section for each bin). Note that the area in the larger particle bins dominates that of the smaller particles, contrary to the long held notion that smaller particles contribute more area than larger particles. One way of interpreting this is that there is an over abundance of larger particles being accreted by the Earth. Also note that there is a cutoff near a particle diameter of 150 μ m. 101
- 6-4: The orbital evolution of a 20 μ m diameter dust particle. From left to right we see the semi-major axis (middle) of the particle orbit decay until it becomes trapped in a first order outer mean-motion resonance with the Earth after about 4500 years. At this point the semi-major axis remains roughly constant while the eccentricity (top) begins to increase. While the orbit is decaying the distance of the particle from the Earth (bottom) decreases. Then, upon capture the particle is initially kept away from the Earth by the resonance. As the eccentricity increases the gap between the Earth and particle narrows until eventually the particle is released from the resonance after being trapped for about 5000 years. . . 102
- 6-5: Evolution of another 20 μ m diameter dust particle which remains trapped in resonance for nearly 10,000 years. Note once again that while in resonance the particle is initially prevented from having a close encounter with the Earth (bottom). However, as the eccentricity (top) increases the particle is brought nearer and nearer until eventually experiencing a close encounter with the Earth and being released from the resonance. 103

Abstract of Dissertation Presented to the Graduate School
of the University of Florida in Partial Fulfillment of the
Requirements for the Degree of Doctor of Philosophy

ACCRETION OF INTERPLANETARY DUST PARTICLES BY THE EARTH

By

STEPHEN JOHN KORTENKAMP

December, 1996

Chairman: Stanley F. Dermott

Major Department: Astronomy

Analysis of micrometeoroid impact craters on the panels of the Long Duration Exposure Facility indicates that the Earth accretes about 3×10^7 kg of interplanetary dust particles (IDPs) from the zodiacal cloud each year. The size distribution of these craters and chemical analysis of collected IDPs suggest that most IDPs accreted by the Earth originate from a single or a few sources in the asteroid belt. Measurements of extraterrestrial ^3He concentrations in deep-sea sediment cores show that the flux of IDPs to the sea floor has varied in the past by a factor of 2–3 with a period near 10^5 years. These recent findings form the motivational basis for the work presented here.

The most abundant sources of dust to be unambiguously linked to the zodiacal cloud are the three asteroid families Eos, Themis and Koronis – the progenitors of the ten-degree and low-latitude dust bands discovered by the Infrared Astronomical Satellite (IRAS). IRAS observations of these dust bands are used to constrain the amount of dust in the zodiacal cloud attributed to Eos, Themis and Koronis. Numerical simulations are used

to model the orbital evolution of dust particles from these three families as well as from other non-family asteroids and from a population of known short period comets. Naturally occurring selection effects are found to bias the terrestrial accretion rate heavily in favor of particles with low geocentric encounter velocities. This bias leads to the result that most IDPs accreted by the Earth probably originate from the Eos, Themis and Koronis families and that probably fewer than 25% of IDPs come from comets.

Models of the historical accretion rate dating back 1.2 million years show that only the accretion rate for Themis particles less than 10 microns diameter varies by a factor of 2–3 with a period near 10^5 years. The phase of these variations, however, does not match the ^3He record. This and other considerations suggest that another unconventional accretion mechanism must be at work. This mechanism may involve accretion from the Earth's resonant dust ring.

CHAPTER 1 INTRODUCTION

In the planetary sciences perhaps nothing is more coveted than samples of extraterrestrial material of known origin. One prominent source of this material is the cache of lunar samples returned during the Apollo and Luna programs, the only sample return missions carried out to date. After nearly three decades of scrutinizing these lunar samples we now have a general understanding of the Moon that is probably more complete than that of any other object in the Solar System except the Earth. Another ample source of material is meteorites, which have been known for several centuries to be extraterrestrial. Unlike the hand-picked lunar samples, however, the origins of meteorites are more controversial. Based on analysis of the Apollo-Luna samples a few meteorites are now recognized as having originated on the Moon. Due largely to the study of the atmosphere and soil of Mars performed by the Viking landers it is also believed that some meteorites have a martian origin. It has recently been suggested that some of these martian meteorites may harbor fossilized evidence of past bacterial life on Mars (McKay *et al.* 1996). The number of lunar and martian meteorites, less than two dozen specimens, is dwarfed in comparison to the thousands of meteorites recovered each year (Binzel *et al.* 1988; Kerridge and Mathews 1989).

Most meteorites are believed to come from limited regions in the asteroid belt corresponding to certain mean motion resonances with Jupiter and secular resonances at the inner edge of the belt (Wisdom 1985; Wetherill 1988). However, linking individual meteorites (or classes of meteorites) with individual asteroids (or classes of asteroids)

has proven to be difficult. The only meteorites to be dynamically and spectroscopically linked to an asteroidal source are the howardite-eucrite-diogenites, many of which are now believed to be fragments of the asteroid 4 Vesta (Binzel and Xu 1993). The precise origin of the most common meteorites, the ordinary chondrites, which constitute 73% of all observed meteorite falls, is unknown (Lipschutz *et al.* 1989; Kerr 1996). The abundant S-class asteroids near the resonances in the inner regions of the main-belt certainly offer a promising source for the ordinary chondrites. However, the reflectance spectra expected of the ordinary chondrite parent bodies do not match the observed spectra of the S-class asteroids (Wetherill 1988). This paradox could be resolved if we had a sample of an S-class asteroid (Wetherill and Chapman 1989). It is our contention that such a sample may be found among the interplanetary dust particles (IDPs) deposited in and collected from the Earth's atmosphere. (Henceforth the term IDP is used to refer to accreted dust particles, not dust particles in space.)

Analyses of hypervelocity micrometeoroid impact craters preserved in lunar material and on the panels of the Long Duration Exposure Facility (LDEF) indicate that the Earth accretes about 3×10^7 kg of IDPs each year (Grün *et al.* 1985; Love and Brownlee 1993). Dust particles in interplanetary space are transported to the Earth primarily due to Poynting-Robertson (P-R) light drag and solar wind drag, which cause their orbits to decay towards the Sun. This mechanism acts on all dust particles in the Solar System regardless of their location. It is quite distinct from the more selective forces that deliver the meteorites from the narrow regions of resonance in the asteroid belt. One might then expect the range in composition of collected IDPs to be broader than that of the meteorites and to be representative of all the dust producing bodies in the Solar System. This is not the case. In fact, the lunar and LDEF cratering records indicate that the size range of dust particles encountering the Earth has an upper limit of about 200 microns diameter

(Grün *et al.* 1985; Love and Brownlee 1993). This particle-size cutoff is indicative of collisionally evolved asteroidal dust, where the collisional lifetime of particles larger than ~ 100 microns is shorter than the time required for their orbits to decay under P-R drag from the asteroid belt to the Earth (Gustafson 1994). Additionally, chemical analysis of IDPs collected from the stratosphere by high-flying aircraft reveals a diversity in chemical composition which is even narrower than that of the meteorites (Flynn 1995). Together these findings suggest that IDPs originate from very limited sources in the asteroid belt. Our work is aimed primarily at identifying what these sources might be.

Any realistic discussion concerning the origin of IDPs implies a prerequisite understanding of the sources of dust in the zodiacal cloud. Chapter 2 provides some background in this area. Much of the material in Chapter 2 is from Grogan *et al.* (1996) and Kortenkamp *et al.* (1996). Chapter 3 contains the derivations of the equations governing accretion. Chapter 4 applies these equations to the results of Chapter 2 to determine relative abundances of IDPs from various sources. Chapter 5 addresses the topic of long term variations in the rate of accretion. The final chapter, Chapter 6, summarizes our findings and offers a discussion of future work, some of which is already in progress.

CHAPTER 2

DUST IN THE ZODIACAL CLOUD

Before Galileo's pioneering use of the astronomical telescope in 1610, humans were limited to observing relatively few Solar System objects – the Sun, the Moon, the five known planets, an occasional “guest star” (comet), and the zodiacal light. In environments with a dark night sky the zodiacal light can be observed by the unaided eye as a faint glow following sunset in the west and preceding sunrise in the east. At low geographic latitudes the zodiacal light can be more than three times as intense as the brightest portions of the Milky Way. Considering this, it is surprising that the earliest observations of the zodiacal light on record in western literature are those of Cassini in 1683. It was at this time that Cassini also correctly theorized that the zodiacal light is due to sunlight being scattered off countless dust particles in interplanetary space, dust particles which collectively make up what we now call the zodiacal cloud.

Dust particles in the zodiacal cloud are acted upon by a number of forces – both gravitational and non-gravitational. The gravitational forces can be separated into a primary force due to the Sun and secondary perturbations due to the planets. These planetary perturbations can be further separated into three categories: (1) secular (or long-period) perturbations; (2) resonant (and/or short-period) perturbations; (3) transient (or scattering) perturbations. The non-gravitational forces include sunlight radiation pressure, solar wind drag and the electromagnetic Lorentz force. In the dynamics modeled in this work we have neglected the Lorentz force. Assuming spherical particles, the effect of sunlight radiation pressure can be separated into two components: (1) a radial component

which acts to negate a portion of the primary gravitational force due to the Sun; (2) a drag component, known as Poynting-Robertson (P-R) light drag. Solar wind drag and P-R drag act to decrease the angular momentum of dust particles, causing their orbits to decay towards the Sun. Typically, dust particles with diameters in the range 1 to 100 microns initially with semi-major axes of about 3AU will be removed from the zodiacal cloud on timescales of 10^4 to 10^6 years. Continuous replenishment of the zodiacal cloud against this depleting action of drag is a task once thought to be performed almost exclusively by comets. Active comets in the inner Solar System, such as Encke, and disrupting comets similar to West and Schwassmann-Wachmann 3 have been proposed as sources (Whipple 1967; Sykes *et al.* 1989; Liou *et al.* 1995). Lately, dust originating in the asteroid belt has attracted much attention (Durda and Dermott 1996). All of these sources probably contribute in some amount.

The advent of Earth-orbiting infrared observatories has provoked considerable interest in the zodiacal cloud. The Earth and the other three terrestrial planets orbit the Sun embedded in the zodiacal cloud. Because of this, all infrared observations made from the Earth or from Earth-orbit necessarily include – some would say are contaminated by – zodiacal emission (as opposed to scattered zodiacal light). In certain infrared wavebands zodiacal emission is the dominant source of extended emission, greater than even the Galaxy. In 1983, three centuries after Cassini recorded his observations, structure was discovered in the zodiacal cloud. Observations made with the Infrared Astronomical Satellite (IRAS) revealed circumsolar, near-ecliptic bands of dust that originate in the asteroid belt and extend to inside the orbit of the Earth (Low 1984). Two pair of prominent dust bands were observed, one pair near $\pm 10^\circ$ ecliptic latitude and one central pair near 0° ecliptic latitude. The 10° band-pair has been linked with the asteroid family Eos and the central band-pair with the two families Themis and Koronis (Dermott *et al.* 1984;

Grogan *et al.* 1996). Further analysis of the IRAS observations has resolved the central band-pair into two components – one attributed to Themis and the other to Koronis (Sykes *et al.* 1989). These three asteroid families remain the only abundant sources to be *unambiguously* linked to dust in the zodiacal cloud. We use models of these dust bands to constrain the relative contributions of asteroids and comets to the zodiacal cloud.

One difficulty in interpreting the structure and origin of the dust bands is the geocentric viewpoint of the IRAS telescope. This viewpoint gives rise to small systematic displacements in the apparent locations of the dust bands which would not arise if the bands were viewed from the Sun. To overcome this and other difficulties a three-dimensional numerical simulation of the zodiacal cloud was constructed to permit the calculation of the distribution of thermal emission that would be produced by any particular distribution of dust particle orbits (Dermott *et al.* 1992). The model (1) includes the effects of planetary perturbations on the dust particle orbits, (2) reproduces the exact viewing geometry of the IRAS telescope, and (3) allows for the eccentricity of the Earth's orbit – all factors which influence the observed structure of the dust bands. We create dust band models to account for the ten-degree band-pair by generating a large population of dust particle orbits (several million orbits are used) with mean proper eccentricity and mean proper inclination equal to those values found from the members of the Eos asteroid family. We model the low-latitude central dust bands in an identical fashion by including dust particles with proper eccentricity and proper inclination corresponding to the Themis and Koronis asteroid families. Line of sight integrations are then made through the composite model dust bands to produce simulated observations which can be directly compared to the IRAS observations. We use a fast Fourier filter on all observations to produce a low frequency smooth background profile and a high frequency dust band profile (Figure 2-1; Dermott *et al.* 1994).

It is important to recognize the distinction between emission in a filtered dust band profile and emission in an unfiltered dust band observation. Previous attempts at determining the contribution of dust band material to the zodiacal cloud were made by comparing filtered IRAS dust band profiles with unfiltered IRAS observations (Love and Brownlee 1992). This approach fails to account for the fact that the filtered dust band profiles represent only the "tip of the iceberg" in terms of the dust band material in the zodiacal cloud (Dermott *et al.* 1994). Much of the emission from the material that constitutes a toroidal dust band is lost to the background emission separated by the filtering process. This effect is exacerbated when a dispersion is imposed on the proper inclination of the dust band material. However, in order to match the observed ecliptic latitudes of the peaks in the ten-degree band-pair a dispersion must be added to the Eos material used in the models (Grogan *et al.* 1996). As the dispersion is increased the latitude of peak intensity decreases and the dust bands become broader. This broadening causes the filter to associate more of the emission from the dust band material with the zodiacal background. Therefore less emission is needed from other sources (cometary dust and/or other asteroidal dust) to account for the total signal in the IRAS observations.

Two dust band models are presented here which are representative of a wide range of possible models. In both models we use spherical 9 micron diameter "astronomical silicate" (Drain and Lee 1984) particles having a density of 2.5 g cm^{-3} . More sophisticated modeling using a range of particle sizes remains to be completed. The first dust band model is composed of material confined to the asteroid belt ($2.0 < a < 3.15 \text{ AU}$). For the dust particles from the Eos family the modeling demands that we use a dispersion in the proper inclination of $2.^\circ 5$ (hereafter the $2.^\circ 5$ model) (Grogan *et al.* 1996). The dispersions on the proper inclination of the Themis and Koronis material are kept equal to the values of their respective asteroid family members ($0.^\circ 3$ and $0.^\circ 1$ respectively).

Figure 2-2 shows the comparison between filtered dust band profiles of this 2.°5 model and the filtered IRAS dust band profiles.

In the 2.°5 model the material is confined to the asteroid belt. However, due to the lunar and LDEF cratering records (Grün *et al.* 1985; Love and Brownlee 1993), measurements made by the dust detectors on board the Galileo and Ulysses spacecraft (Grün 1994) and the existence of the Earth's resonant dust ring (Dermott *et al.* 1994; Reach *et al.* 1995) we know that some fraction of asteroidal dust reaches the inner Solar System. Results from a second dust band model that allows material to be distributed from the asteroid belt into the inner Solar System indicate that the latitudes of peak intensity of the model ten-degree band-pair increase due to a parallax effect. In order to maintain the band-pair at the latitude observed by IRAS, the dispersion in proper inclination must be increased (Grogan *et al.* 1996). Consequently, a second model using Eos particles with a dispersion in proper inclination of 3.°5 is constructed (hereafter the 3.°5 model). In the 3.°5 model the Eos material is distributed from the asteroid belt to the Sun. The particle number density for this Eos material varies with the inverse of the heliocentric distance r . This $1/r$ dependence is a result of orbital decay due to P-R light drag. In the 3.°5 model the central dust bands are modelled the same as in the 2.°5 model, that is, the Themis and Koronis material is confined to the asteroid belt with proper elements and proper element dispersions kept equal to the values of the two asteroid families. Figure 2-3 compares the filtered dust band profiles of the 3.°5 model with the filtered IRAS dust band profiles.

Figure 2-4 compares unfiltered simulated observations from the 2.°5 and 3.°5 models with an unfiltered IRAS observation. The same surface area of dust is used in both models; however, the emission from the 3.°5 model is greater than the emission from the 2.°5 model. This is because the material in the 3.°5 model is closer to the Sun,

hence warmer, and closer to the Earth. The difference in the peak intensity between a given unfiltered model observation and the unfiltered IRAS observation is indicative of the dust band contribution to the entire zodiacal cloud. The $2.^\circ 5$ model bands represent about 5% of the peak flux detected by IRAS. The $3.^\circ 5$ model bands represent about 25% of the peak flux detected by IRAS. Table 2-1 lists the amount of Eos, Themis and Koronis material we use in our models in terms of the surface area contribution from each family. Also shown in Table 2-1 is the contribution from each family to the peak flux observed in the IRAS $25\mu\text{m}$ waveband. The contributions shown in Table 2-1 for the Eos family (4% to 21%) are about a factor of 40 higher than the estimates found by Love and Brownlee (1992; 0.1% to 0.5%) for the contribution to the zodiacal cloud from material in ten-degree dust bands.

The existence of the dust bands only indicates that dust is being produced by families in the asteroid belt, not necessarily that this dust is reaching the Earth. However, the lunar and LDEF cratering records and the in-situ measurements made by the dust detectors on board the Galileo and Ulysses spacecraft suggest that asteroidal dust is being transported to the inner Solar System (Grün *et al.* 1985; Love and Brownlee 1993; Grün *et al.* 1994). Furthermore, observations of the zodiacal cloud made by the Cosmic Background Explorer satellite (COBE) confirm the existence of the Earth's resonant ring of asteroidal dust (Dermott *et al.* 1994; Reach *et al.* 1995). Comparison between the COBE observations and models of this dust ring suggests that the asteroidal contribution to the entire zodiacal cloud can range from about 10% to as high as 100%. The large range arises from uncertainty in the slope of the size-frequency distribution of the particles being modeled (Jayaraman and Dermott 1996). Therefore we use the broad range shown in Table 2-1 for the contribution of asteroid families in the source region (5% to 25%) as a representation of the probable asteroid family contribution to the population of Earth-crossing dust particles in the zodiacal cloud.

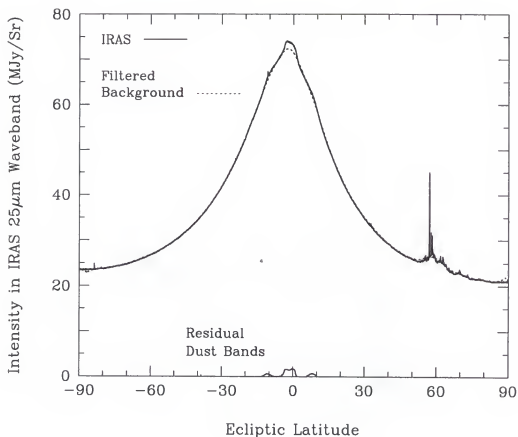


Figure 2-1: IRAS observation of the zodiacal cloud in the $25\mu\text{m}$ infrared waveband (solid upper curve). This observation was made at 90° solar elongation angle (the angle between the telescope pointing direction and the Earth-Sun line) in the direction leading the Earth in its orbit when the planet was at an ecliptic longitude of 293° . The dust bands can be seen as projecting "shoulders" near $\pm 10^\circ$ and 0° latitude. The structure around 60° latitude is due to dust in the plane of the Galaxy. By applying a Fourier filter to the IRAS observation a smooth background profile (underlying dashed curve) is separated from a high frequency dust band profile (solid lower curve). This filtered high frequency dust band profile is merely a residual representing the "tip of the iceberg" in terms of the dust band material in the zodiacal cloud.

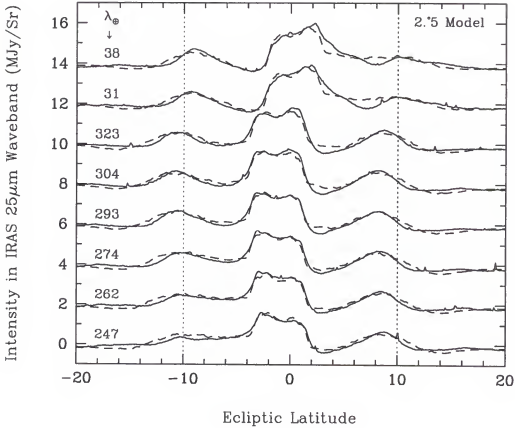


Figure 2-2: Filtered IRAS dust band profiles (solid lines) for eight different longitudes of the Earth (λ_{\oplus}). All profiles were made at 90° solar elongation angle in the direction leading the Earth in its orbit. Model dust bands were constructed using particles from the Themis and Koronis families for the central band-pair and the Eos family for the 10° band-pair. A dispersion of 2.5° was imposed on the proper inclination of the Eos material in this model. All of the material in this model was confined to the asteroid belt. Eight simulated profiles (dashed lines) which mimic the IRAS $25\mu\text{m}$ infrared waveband were made through these model dust bands at the same longitudes and elongation angle as the IRAS profiles. These simulated profiles were filtered in a fashion identical to that used to generate the IRAS profiles. Dashed vertical lines are placed at $\pm 10^\circ$ for reference. All profiles have an amplitude of around 2 MJy/Sr but are staggered in the figure for convenience.

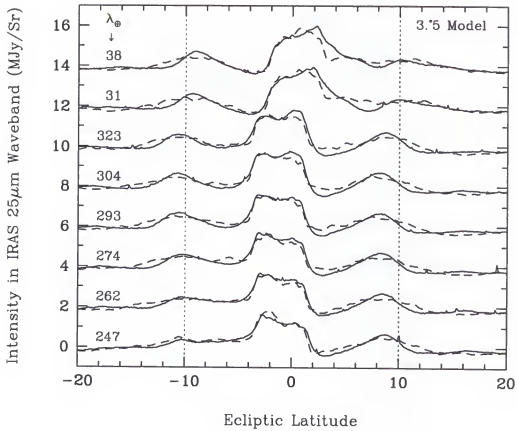


Figure 2-3: Same as in Figure 2-2 except these filtered model dust band profiles (dashed lines) are for the 3.5 model in which the Eos material is distributed from the asteroid belt to the Sun.

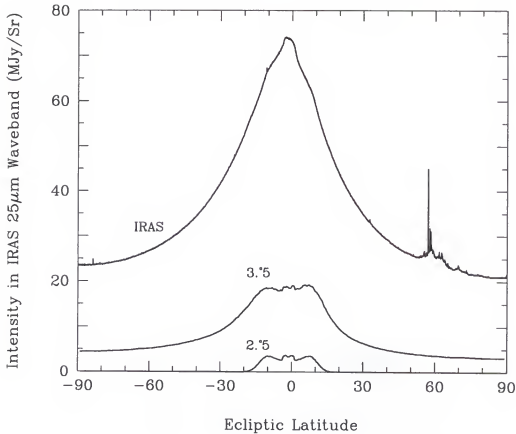


Figure 2-4: Unfiltered IRAS observation shown in Figure 2-1. The lower and middle curves are simulated *unfiltered* profiles mimicking the IRAS $25\mu\text{m}$ infrared waveband taken through two different dust band models. Each of these dust band models was constructed using particles from only the three asteroid families Eos, Themis and Koronis. The model profile labeled 2.5 uses Eos particles having a 2.5° dispersion in proper inclination and confines all particles to the asteroid belt. The model profile labeled 3.5 is constructed using Eos particles with a 3.5° dispersion in proper inclination and by allowing the Eos material to stretch from the asteroid belt to the inner Solar System. The difference in the peak intensity between a given model profile and the IRAS profile indicates the dust band contribution to the entire zodiacal cloud, listed in Table 2-1.

Table 2-1: The area of dust contributed from each family is the same in both the 2.°5 and the 3.°5 models. However, in the 3.5° model material is distributed between the asteroid belt and the Sun whereas in the 2.°5 model the material is confined to the asteroid belt.

Asteroid Family	Area of Dust Used in Models (10 ⁹ km ²)	Fraction of Peak Infrared Flux Observed in IRAS 25μm Waveband	
		2.°5 Model	3.°5 Model
Eos	6.00	4%	21%
Themis	0.53	0.5%	2%
Koronis	0.53	0.5%	2%
Total	7.06	5%	25%

CHAPTER 3 THE MECHANICS OF ACCRETION

As the Earth orbits the Sun, it sweeps up dust particles from the zodiacal cloud. The rate at which particles are captured is dependent on three things: (1) the average spatial density of particles on Earth-crossing orbits; (2) the geocentric encounter velocity of the particles; (3) the effective cross-section of the planet. In the sections below we step through the derivations of these three key elements. We use Kessler's (1981) formulation for the spatial density and Öpik's (1951) original derivation of the effective cross-section. We then follow Kessler (1981) in combining these three elements to form the capture rate, N/t , expressed as

$$N/t = SV_o\sigma_{eff} \quad (3.1)$$

where S is the average spatial density of particles, V_o is the geocentric encounter velocity and σ_{eff} is the effective cross-section.

Average Spatial Density

The orbit of a particle in the Solar System can be completely characterized with respect to a designated reference system by a set of five orbital elements: the semi-major axis (a), eccentricity (e), inclination (I), longitude of ascending node (Ω), and the argument of pericenter (ω). Sometimes it is preferable to refer to a dog-leg angle known as the longitude of pericenter, defined as $\tilde{\omega} = \Omega + \omega$. Under certain conditions four of these five elements ($e, I, \Omega, \tilde{\omega}$) may in turn be separated into what are known as forced elements ($e_f, I_f, \Omega_f, \tilde{\omega}_f$) and proper elements ($e_o, I_o, \Omega_o, \tilde{\omega}_o$). The proper elements are

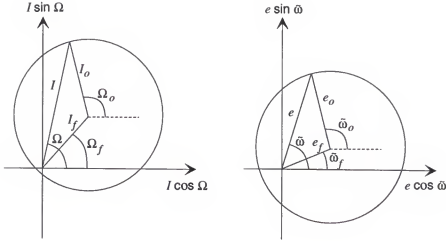


Figure 3-1: Demonstration of the concept of forced and proper orbital elements.

the stable long-term averages that remain after removal of periodic secular variations, which are the forced elements. These forced and proper elements combine vectorally as shown in Figure 3-1 to give the total, or osculating elements $(e, I, \Omega, \tilde{\omega})$.

The gravitational perturbations acting on a small body in orbit about the Sun progressively precess Ω_o and ω_o . Over sufficiently long time intervals the distribution of these two parameters becomes essentially random. Excellent examples of this can be seen in the distributions of asteroid family members when plotted in $(e \cos \tilde{\omega}, e \sin \tilde{\omega})$ or $(I \cos \Omega, I \sin \Omega)$ space. Figure 3-2 shows an example of this for the members of the Themis asteroid family. Comparison between the schematic of Figure 3-1 and Figure 3-2 shows that the distributions of the asteroids are displaced from the origin due to the forced elements and that the radius of the distributions indicates the proper elements of the asteroids. The population of dust particle orbits used in this work are assumed to come from the population of asteroids and comets. Therefore, for these calculations we will assume that all values of the two proper elements Ω_o and ω_o are equally probable. Under this assumption the spatial density of particles will not vary with longitude and

will only have a radial and latitude dependence. In terms of the derivation of the capture rate, this also means that while the precession rates of Ω_o and ω_o may not be strictly constant, we can assume that they are.

Following the notation of Kessler (1981) the average spatial density can be written as

$$S(R, \beta) = s(R) \cdot f(\beta). \quad (3.2)$$

Here the radially dependent term, $s(R)$, is the spatial density at a distance R from the central body averaged over all latitudes and the latitude dependent term, $f(\beta)$, is the ratio of the spatial density at latitude β to the spatial density averaged over all latitudes. The function $f(\beta)$ is independent of R for a particular orbit and is only a function of inclination.

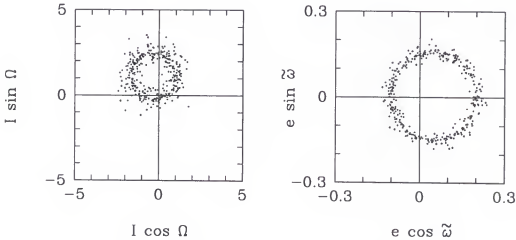


Figure 3-2: Osculating orbital elements for 357 members of the Themis asteroid family.

There are two ways to visualize $S(R, \beta)$; the first is to think of it as the probability of finding a single body in a given volume element if you look at random times over an interval long enough for the particle orbit to completely precess in Ω_o and ω_o . This is

useful when studying Earth-crossing asteroids to determine the long term probability of impact. The second visualization technique is to assume an entire population of particles all sharing a common a, e_o, I_o but with randomly oriented Ω_o and $\tilde{\omega}_o$. Then $S(R, \beta)$ represents the average spatial density of particles in the population at the position (R, β) . This second approach allows us to describe the spatial density as it varies with latitude in an asteroidal dust band. While the equations are derived using a single particle orbit they can be used to deal with an entire population of particles.

In general, for a single particle, the average spatial density S is represented by

$$S = \frac{\Delta t}{T \Delta U} \quad (3.3)$$

where Δt is the time spent by the particle in the volume element ΔU over time T . Time T must be long enough for the particle to have passed through all regions of space accessible to it. For the radial dependence T is simply the orbital period. For the latitude dependence T is the time required for complete precession of the argument of pericenter, ω .

Radial Dependence

Following Figure 3-3, assume a particle is at a distance R from the Sun and moving along an elliptical orbit with perihelion q and aphelion q' such that $q \leq R \leq q'$. Imagine then a spherical shell of radius R and thickness ΔR . The volume of this shell is given by

$$\Delta U = 4\pi R^2 \Delta R. \quad (3.4)$$

The particle will pass through this shell twice for each revolution in its orbit. The time spent in the shell per revolution is then

$$\Delta t = 2\Delta R/V_r \quad (3.5)$$

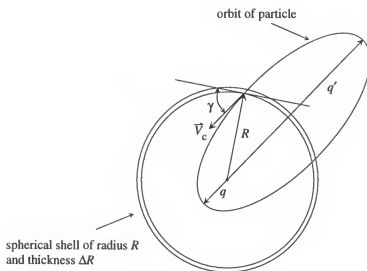


Figure 3-3: Radial dependence of the spatial density.

where V_r is the magnitude of the radial velocity of the particle, which is the same for inbound and outbound trajectories. From Kepler's third law the orbital period is

$$T = 2\pi \left(\frac{a^3}{\mu_\odot} \right)^{1/2} \quad (3.6)$$

where $a = (q + q')/2$ and $\mu_\odot = GM_\odot$. (Note that if distance is measured in astronomical units and time in years then $\sqrt{\mu_\odot} \equiv 2\pi \text{ AU}^3 \text{ yr}^{-2}$.)

The heliocentric velocity of the particle (V_c in Figure 3-3) is

$$V_c = \mu^{1/2} \left(\frac{2}{R} - \frac{1}{a} \right)^{1/2} \quad (3.7)$$

and the radial component, V_r , is then

$$V_r = V_c \sin \gamma \quad (3.8)$$

where γ is the angle between the velocity vector \vec{V}_c and the tangent of the spherical shell measured in the plane of the particle orbit. Now let \vec{V}_q and $\vec{V}_{q'}$ be the velocity of the particle at q and q' respectively and let V_t be the tangential component of V_c . Then by

conservation of angular momentum we have

$$V_q q = V_t R = V_c \cos \gamma R \quad (3.9)$$

and

$$V_{q'} q' = V_t R = V_c \cos \gamma R \quad (3.10)$$

so that

$$\cos^2 \gamma = \left(\frac{V_q q}{V_c R} \right) \left(\frac{V_{q'} q'}{V_c R} \right) = \frac{q q'}{R^2} \cdot \frac{V_q V_{q'}}{V_c^2}. \quad (3.11)$$

With equation (3.7) above (letting $R = q$ for V_q and $R = q'$ for $V_{q'}$) and canceling the common μ terms we have

$$\cos^2 \gamma = \frac{q q'}{R^2} \cdot \frac{1}{\left(\frac{2}{R} - \frac{1}{a} \right)} \left[\left(\frac{2}{q} - \frac{1}{a} \right) \left(\frac{2}{q'} - \frac{1}{a} \right) \right]^{1/2} \quad (3.12)$$

which simplifies to

$$\cos^2 \gamma = \frac{q q'}{R(2a - R)} \left[\frac{(2a - q)(2a - q')}{q q'} \right]^{1/2}. \quad (3.13)$$

Then with $2a - q = q'$ and $2a - q' = q$ we are left with

$$\cos^2 \gamma = \frac{q q'}{R(2a - R)} \quad (3.14)$$

or, after invoking the trigonometric identity $\sin^2 \theta + \cos^2 \theta = 1$,

$$\sin \gamma = \left[1 - \frac{q q'}{R(2a - R)} \right]^{1/2}. \quad (3.15)$$

Using equations (3.7) and (3.15) we can rewrite equation (3.8) as

$$V_r = \left[\mu \left(\frac{2}{R} - \frac{1}{a} \right) \left(1 - \frac{q q'}{R(2a - R)} \right) \right]^{1/2}. \quad (3.16)$$

Finally, by combining equations (3.4), (3.5), (3.6) and (3.16) we can express equation (3.3) as

$$s(R) = \frac{2\Delta R}{\left[\mu \left(\frac{2}{R} - \frac{1}{a} \right) \left(1 - \frac{q q'}{R(2a - R)} \right) \right]^{1/2}} \cdot \frac{1}{2\pi \left(\frac{a^3}{\mu} \right)^{1/2}} \cdot \frac{1}{4\pi R^2 \Delta R}. \quad (3.17)$$

Reducing and noting that $2a = q + q'$ we are left with the radial dependence of the spatial density

$$s(R) = \frac{1}{4\pi^2 R a [(R - q)(q' - R)]^{1/2}}. \quad (3.18)$$

Latitude Dependence

The latitude dependence of the spatial density, $f(\beta)$, is due to the inclination of an orbit with respect to a reference plane and the rate of change of the argument of pericenter. Imagine a single particle at an arbitrary distance between R_1 and $R_1 + \Delta R$ from the Sun. The particle is stationary in its orbit but the argument of pericenter precesses at a constant rate, implying that all values of the argument of pericenter are equally likely. The path of this particle is a circle of radius R_1 . This circular path and the orbit of the particle are in the same plane and inclined to a reference plane by the orbital inclination. By definition $f(\beta)$ is the ratio of the spatial density at latitude β to the spatial density averaged over all latitudes. Since the particle is fixed between R_1 and $R_1 + \Delta R$ the probability of it being in the spherical shell is unity. Then the spatial density in the shell averaged over all latitudes is this probability divided by the volume of the shell, or

$$s'(R_1) = \frac{1}{4\pi R_1^2 \Delta R}. \quad (3.19)$$

Now the spatial density between latitude β and $\beta + \Delta\beta$ is given by equation (3.3) above except in this case Δt is the time the particle is between β and $\beta + \Delta\beta$, T is the period of one revolution in argument of pericenter, and ΔU is the volume between β and $\beta + \Delta\beta$ in the spherical shell of thickness ΔR .

If the argument of pericenter is moving with constant angular velocity $\dot{\omega}$ and α is the angle between the path of the object and the line of constant latitude β , as shown in Figure 3-4, then the particle will pass through the latitude region of thickness $\Delta\beta$ twice

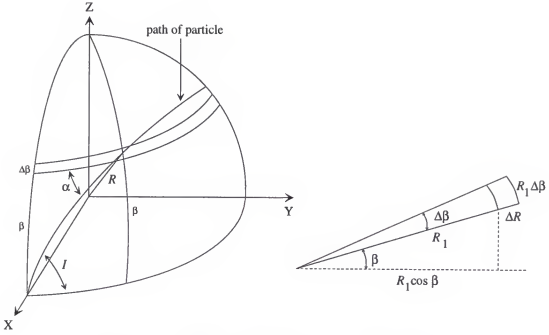


Figure 3-4: Latitude dependence of the spatial density and volume of latitude element of spherical shell.

each revolution with velocity $\dot{\omega} \sin \alpha$. So the time spent in the volume element is

$$\Delta t_1 = \frac{2\Delta\beta}{\dot{\omega} \sin \alpha}. \quad (3.20)$$

The time for one revolution of pericenter is

$$T_1 = \frac{2\pi}{\dot{\omega}} \quad (3.21)$$

and, from Figure 3-4, the volume between β and $\beta + \Delta\beta$ in the spherical shell of thickness ΔR is

$$\Delta U_1 = 2\pi R_1^2 \cos \beta \Delta\beta \Delta R. \quad (3.22)$$

Therefore the spatial density at R_1 and β , given that the object is between β and $\beta + \Delta\beta$ is found from equations (3.20), (3.21) and (3.22),

$$S'(R_1, \beta) = \frac{\Delta t_1}{T_1 \Delta U_1} = \frac{1}{2\pi^2 R_1^2 \sin \alpha \cos \beta \Delta R} \quad (3.23)$$

where $0 < \beta < I$. By definition $f(\beta)$ is the ratio of equation (3.23) and (3.19)

$$f(\beta) = \frac{4\pi R_1^2 \Delta R}{2\pi^2 R_1^2 \sin \alpha \cos \beta \Delta R} \quad (3.24)$$

or simplifying

$$f(\beta) = \frac{2}{\pi \sin \alpha \cos \beta}. \quad (3.25)$$

From Figure 3-4 the sine formula of spherical trigonometry gives

$$\frac{\sin(\frac{\pi}{2} + \alpha)}{\sin \frac{\pi}{2}} = \frac{\sin(\frac{\pi}{2} - I)}{\sin(\frac{\pi}{2} - \beta)} \quad (3.26)$$

which, after squaring and noting that $\sin(\frac{\pi}{2} \pm \theta) = \cos \theta$, can expressed as

$$\cos^2 \alpha \cos^2 \beta = \cos^2 I. \quad (3.27)$$

Two applications of the trigonometric identity $\sin^2 \theta + \cos^2 \theta = 1$ allows us to write

$$\sin \alpha \cos \beta = (\sin^2 I - \sin^2 \beta)^{1/2}. \quad (3.28)$$

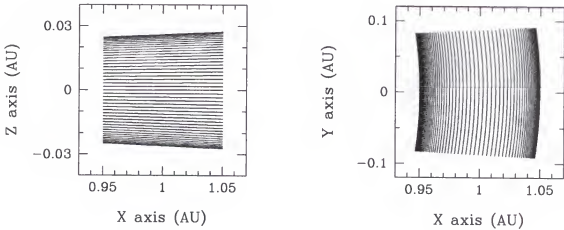


Figure 3-5: Latitude (left) and radial (right) average spatial density distributions. An orbit with $a = 1$, $e = 0.05$ and $I = 1.5$ was used, the Sun is at the origin off the figure to the left.

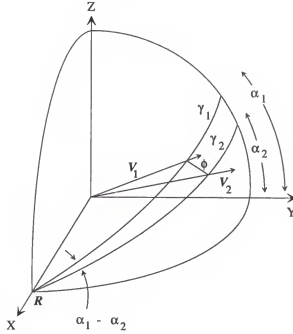


Figure 3-6: Velocity vector relationship for determining encounter velocity.

Finally, the average spatial density at any particular distance R and latitude β , following from equation (3.2) is the product of equations (3.18) and (3.25), which, after incorporating (3.28), is

$$S(R, \beta) = \frac{1}{2\pi^3 R a [(\sin^2 I - \sin^2 \beta)(R - q)(q' - R)]^{1/2}} \quad (3.29)$$

where $q < R < q'$ and $0 < \beta < I$. From Figure 3-5 we see that the enhancement at the extremes in latitude are similar to the structure of an idealized dust band.

Relative Encounter Velocity

The relative encounter velocity is given by the vector difference

$$\vec{V}_o = \vec{V}_1 - \vec{V}_2 \quad (3.30)$$

where V_1 and V_2 are the velocities of the particle and planet with respect to the central body as given by equation (3.7). The magnitude of the encounter velocity is then

$$V_o^2 = V_1^2 + V_2^2 - 2V_1 V_2 \cos \phi \quad (3.31)$$

where ϕ is the angle between the two velocity vectors. Figure 3-6 shows the two vectors in a stationary coordinate system centered at the point of intersection. The X-axis points towards the central body. The Y-axis is along a line of constant latitude. The Y-Z plane is tangent to the spherical shell of Figure 3-3. The angle γ is defined as the angle between the Y-Z plane and the velocity vector as measured in the plane of the orbit. From the cosine formula of spherical trigonometry and Figure 3-6 we have

$$\begin{aligned}\cos \phi = & \cos \left(\frac{\pi}{2} - \gamma_1 \right) \cos \left(\frac{\pi}{2} - \gamma_2 \right) \\ & + \sin \left(\frac{\pi}{2} - \gamma_1 \right) \sin \left(\frac{\pi}{2} - \gamma_2 \right) \cos (\alpha_1 - \alpha_2)\end{aligned}\quad (3.32)$$

or

$$\cos \phi = \sin \gamma_1 \sin \gamma_2 + \cos \gamma_1 \cos \gamma_2 \cos (\alpha_1 - \alpha_2) \quad (3.33)$$

where γ and α are found using (3.14) and (3.27) above. Each of these angles can be positive or negative, resulting in a total of four different encounter velocities from the 16 possible combinations. For our calculations we use the average of these four encounter velocities.

Gravitational Cross-Section

As particles approach the Earth their trajectories are deflected towards the planet by its gravitational field. Öpik (1951) demonstrated that this deflection results in a gravitationally enhanced cross-section of the planet.

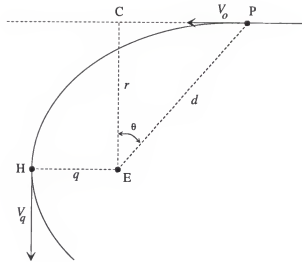


Figure 3-7: Hyperbolic deflection of a particle encountering the Earth.

In Figure 3-7 a particle at P is a distance d from the Earth at E. The particle is moving with velocity V_o relative to the Earth and is deflected by the gravitational field of the planet. The deflection is hyperbolic and in the plane PEH with a distance of closest approach to the Earth of q . The projected unperturbed path of the particle comes closest to the Earth at the point C, a distance r from the planet, r being referred to as the target radius. Now the effective encounter cross-section is

$$\sigma_{eff} = \pi r^2. \quad (3.34)$$

Meaning that if the unperturbed path of the particle is projected to pass within r then the actual path of the particle will pass within q .

With the velocity of the particle at closest approach given by V_q and recognizing that $\cos \theta = \frac{r}{d}$, conservation of angular momentum requires that

$$dV_o \cos \theta = rV_o = qV_q \quad (3.35)$$

so that

$$\sigma_{eff} = \pi r^2 = \pi q^2 \left(\frac{V_q}{V_o} \right)^2. \quad (3.36)$$

The effective encounter cross-section σ_{eff} is equal to πq^2 times the ratio of kinetic energy at the pericenter to that at the starting point.

Note that by conservation of energy

$$V_q^2 = V_o^2 + V_e^2 \quad (3.37)$$

where V_e is the velocity required to escape from the distance q to d . Then equation (3.36) becomes

$$\sigma_{eff} = \sigma \left(1 + \frac{V_e^2}{V_o^2} \right) \quad (3.38)$$

where $\sigma = \pi q^2$. For the purposes of our work we want the particle to be not only deflected but actually captured, so q is taken to be the radius of the Earth extending out to 100 km altitude in the atmosphere.

The velocity required to escape from the distance q to d is given by

$$V_e^2 = 2\mu_{\oplus} \left(\frac{1}{q} - \frac{1}{d} \right) \quad (3.39)$$

where G is the universal gravitational constant and $\mu_{\oplus} = GM_{\oplus}$ is the mass of the Earth.

We assume as a limitation for the target radius, r in Figure 3-7, that

$$q \leq r \leq D_a \quad (3.40)$$

where D_a is the radius of the so called "sphere of action" associated with the planet. The sphere of action around a planet is a vague indication of where the influence of the gravitational field of the planet becomes more important than the influence of the

gravitational field of the Sun. Öpik's (1951) sphere of action for the Earth is $D_a = 0.0115$ AU = 1.72×10^6 km. If we look at only the distance terms in equation (3.39) notice that

$$\frac{\left(\frac{1}{q} - \frac{1}{d}\right)}{\frac{1}{q}} = 1 - \frac{q}{d}. \quad (3.41)$$

Then if $d = D_a$ and $q = R_{\oplus} + 100$ km = 6470 km we have $q/d \simeq 4 \times 10^{-3}$. Thus for our purposes it is allowable to let $d \rightarrow \infty$ so that equation (3.39) becomes

$$V_e^2 = \frac{2\mu_{\oplus}}{q}. \quad (3.42)$$

With $G = 6.67 \times 10^{-20}$ km³ kg⁻¹ s⁻², $M_{\oplus} = 5.97 \times 10^{24}$ kg and $q = 6470$ km we have $V_e = 11.1$ km s⁻¹.

The formulation of this effective cross-section is a two-body approximation, but for very low encounter velocities perturbations from other bodies (the Sun and the Moon) may become important. Wetherill and Cox (1985) have shown numerically that for extremely low encounter velocities $V_o/V_e \leq 0.02$ the effective capture cross-section formula shown above is still valid – albeit in a statistical sense – but has an upper limit of $\sigma_{eff}/\sigma = 3000$.

Capture Rate

The capture rate, equation (3.1), can now be calculated from equations (3.29), (3.31), (3.38) and their respective supporting equations. It is given by

$$N/t = \frac{V_o \sigma_{eff}}{2\pi^3 R a [(\sin^2 I - \sin^2 \beta)(R - q)(q' - R)]^{1/2}} \quad (3.43)$$

This is the method that we use to determine the capture rates in the next two chapters of this work. The capture rate is expressed in the units Gyr⁻¹, which represents the number of captures per billion years per particle on a similar orbit. To convert this into a particle influx we would multiply the total number of particles on similar Earth-crossing orbits.

Note the difference between the latitude β and the term β_f , which represents the ratio of radiation pressure to gravitational force on a particle. The subscript f is included to distinguish between the two variables.

Strictly speaking, when calculating the velocity of the dust particles, equation (3.7) must be multiplied by the factor $\sqrt{1 - \beta_f}$ in order to account for the force due to radiation pressure. This slightly lower particle velocity will result in a slightly higher encounter velocity because of the vector combination of equation (3.31). Therefore, the effective capture cross-section will be smaller. However, the encounter velocity term in the equation of the capture rate (3.43) tends to compensate for the smaller cross-section.

CHAPTER 4

THE ORIGIN OF IDPS

Earth-crossing orbits of typical asteroidal and cometary dust particles have similar distributions in ecliptic inclination. The drag forces (P-R drag and solar wind drag) acting on dust particles that cause their semi-major axes to decay towards the Sun also act to reduce their proper eccentricities. As a result asteroidal particles have Earth-crossing orbits that are nearly circular ($e \lesssim 0.05$). Cometary particles however, tend to have Earth-crossing orbits with considerable eccentricities ($e \gtrsim 0.3$). The disparity in eccentricities between the two Earth-crossing populations results in lower geocentric encounter velocities for asteroidal particles and thus larger effective capture cross-sections compared to cometary particles. Flynn (1990) noted that this may imply an enhancement of asteroidal over cometary dust near the Earth. Flynn also showed that any low inclination asteroidal dust particles encountering the Earth would see an enhanced capture cross-section as much as two orders of magnitude larger than the actual geometric cross-section. It was later suggested that two of the largest families in the asteroid belt – Themis and Koronis – which have low ecliptic inclinations and are known dust producers, may contribute significantly to the IDPs (Love and Brownlee 1992; Kortenkamp *et al.* 1996a).

In this chapter we investigate accretion of dust particles from various sources. We consider the following three parent body populations: (1) short period comets with semi-major axes inside the orbit of Jupiter, referred to as Jupiter family comets, (2) main-belt asteroids that do not belong to the Eos, Themis or Koronis families, referred to as non-family asteroids, and (3) asteroids belonging to the Eos, Themis and Koronis families.

Initial Parent Body Population

Our initial population of comets consists of a set of 118 Jupiter family comets with semi-major axes of $a < 4.5\text{AU}$. Figure 4-1 shows the distribution of osculating inclination versus semi-major axis for these comets. Most of these comets fall below 35° inclination. Figure 4-2 shows the distribution of osculating eccentricity versus semi-major axis for these comets. In this plot the dashed line is representative of an inner boundary of the Jupiter-crossing regime. The eccentricity of Jupiter's orbit oscillates between about $e = 0.062$ and $e = 0.025$ with a period near 65,000 years. The larger of these two eccentricity values was used to determine the lower limit of Jupiter's perihelion, $q = 4.88\text{AU}$. We then reduced this value further by the Jovian "sphere of action," $D_a \simeq 0.365\text{AU}$ (Öpik 1951). All of the comets shown on this plot have aphelion greater than this lower limit to the Jupiter-crossing boundary. The two histograms in Figure 4-3 are simply an alternate method of showing the same information plotted in Figures 4-1 and 4-2. The upper histogram bins the comets in 0.5° inclination intervals and shows that most comets in this set have inclinations below 20° with a small tail in the distribution out to around 35° . The lower histogram bins the comets in 0.05 eccentricity intervals. Nearly all of the comets have eccentricities between 0.3 and 0.8, with only four comets having eccentricities below 0.2.

Our initial asteroidal population, both family and non-family, consists of a complete set of bright main-belt asteroids with absolute visual magnitude $H < 11$, a total of 1053 asteroids. Figure 4-4 shows the proper inclination distribution of these asteroids up to 35° . The asteroid family Eos is visible at about 10° and 3AU. The Themis and Koronis families appear as two clusters with low inclination at about 3.1 and 2.9AU respectively. The Kirkwood gaps corresponding to the 3:1, 5:2 and 2:1 mean motion

resonances with Jupiter are evident at about 2.5, 2.8 and 3.3AU respectively. Figure 4-4 is at the same scale as the cometary plot of Figure 4-1 except with a shift of 1AU in semi-major axis. Histograms of the inclination distribution of these asteroids are shown in Figure 4-5 where we have separated the asteroid family members from the non-family asteroids. We see that the Themis and Koronis families, falling at or below 2° inclination, contain a large majority of the low inclination asteroids in the main-belt. The Eos family is also quite large, containing more than half of all the asteroids near 10° . These are the three largest families in the asteroid belt. The next largest, Maria, is visible at about 15° . The remaining non-family asteroid population has a fairly smooth distribution with most asteroids falling inside of 25° proper inclination and a small tail extending out to about 35° . Comparison of the lower histogram in Figure 4-5 with the comets in the upper histogram in Figure 4-3 shows them each to have similar inclination distributions; however, the eccentricity distributions of the two populations are quite different. Figure 4-6 shows that virtually all of the asteroids in the population fall below 0.3 in eccentricity. For the purposes of comparison Figure 4-6 is at the same scale as the cometary plot of Figure 4-2 with a shift of 1AU in semi-major axis. Histograms of the inclination distribution of these asteroids are shown in Figure 4-7. Comparing the cometary histograms (Figure 4-3) with the asteroidal histograms (Figure 4-7) reveals the fundamental difference between the two populations. While only four asteroids have eccentricities significantly above 0.3, all *except* four comets have eccentricities above 0.3.

Generation and Evolution of Dust Particle Orbits

The orbital evolution of cometary and asteroidal dust particles migrating past the Earth under the influence of P-R drag and solar wind drag was modeled for dust particles with a ratio of radiation pressure to gravitational force, β_f , of 0.0469. For spherical dust

particles composed of "astronomical silicate" (Drain and Lee 1984) and having a density of 2.5 g cm^{-3} this β_f value corresponds to a diameter of 10 microns.

Using the RADAU fifteenth-order integrator program with variable time steps taken at Gauss-Radau spacing (Everhart 1985) we perform direct numerical integration of the full equations of motion for these dust particles. Our simulations include seven planets (Mercury and Pluto are excluded) and account for both P-R drag and solar wind drag. The average force due to the solar wind drag is taken to be 30% of the P-R drag force, varying with the 11-year solar cycle from 20% to 40% (Gustafson 1994).

The orbit of each comet in our initial population was essentially transformed into a particle orbit in a one-to-one mapping of the orbital elements. The orbits of these cometary dust particles were then integrated with the RADAU code for the equivalent of 35,000 years. At 500 year intervals we sampled the population for any Earth-crossing orbits. The orbital elements for these Earth-crossing cometary particles are shown in Figures 4-8 and 4-9. The evolution of particles from particular comets is evident by the obvious tracking seen in these figures. This is misleading however because it gives the impression that the cometary dust in the zodiacal cloud comes from these known comets. The conventional theory is that the collisional disruption and disintegration of Jupiter family comets sustains the cometary component of the zodiacal cloud, not the activity of observable comets. It is necessary, therefore, to use our set of Earth-crossing cometary orbits as an indication of the distribution of cometary orbital elements, not as a strict representation of these orbital elements. The mean and dispersion of the orbital element distributions shown in Figures 4-8 and 4-9 are used to create a random gaussian distribution of Earth-crossing cometary orbits that is devoid of the tracking of individual cometary orbits. These smoothed distributions are shown in Figures 4-10 and 4-11. The Earth-crossing cometary orbits span about 3AU in semi-major axis, 35° in inclination and

have eccentricities of 0.2 or greater. Comparison with Figures 4-1 and 4-2 shows that the distributions in inclination and eccentricity of these evolved Earth-crossing cometary orbits have not changed much from the parent population.

The initial distribution for the non-family asteroidal dust particles was taken from our set of 1053 bright asteroids by excluding 173 members of the Eos, Themis and Koronis families. Each of the remaining 880 asteroids was essentially transformed into a dust particle in a one-to-one mapping of the orbital elements. We analytically integrated the proper eccentricities of these orbits beginning with the semi-major axis of the parent asteroid and ending near a semi-major axis of 1AU. The decay of proper eccentricity with semi-major axis under the influence of P-R drag is found from Dermott *et al.* (1994b) and given by

$$\frac{de_o}{da} = \frac{5e_o(1 - e_o^2)}{2a(2 + 3e_o^2)}. \quad (4.1)$$

There are at least two reasons for using the analytical method for these particles, as opposed to direct calculation with RADAU. The forced elements of dust particle orbits vary with time and with semi-major axis. RADAU is useful in determining the forced elements of asteroidal particles at a particular semi-major axis and at a particular time and in tracking the forced elements as the particles evolve to a different semi-major axis. However, the non-family asteroidal orbits have a broad range in initial semi-major axes and therefore require a range in times to evolve into Earth-crossing orbits. The forced elements of each of the Earth-crossing non-family asteroidal orbits would be different. Also, the forced elements of particles become particularly important when they are comparable with the proper elements. For the large range in proper inclination of the non-family asteroidal orbits, reaching as high as 35°, a forced inclination of 1.°5 (the typical value) is insignificant. The orbits of these Earth-crossing non-family asteroidal

particles are shown in Figures 4-12 and 4-13. Due to their lower initial eccentricities, and the further reduction of their proper eccentricities by P-R drag these Earth-crossing asteroidal orbits are confined to a narrow range in semi-major axis around 1AU. However, their inclinations are unaffected and retain the same distribution as the parent asteroids. Comparison of the Earth-crossing cometary orbits in Figure 4-11 with the Earth-crossing asteroidal orbits in Figure 4-13 shows that the disparity in the distribution of eccentricities between the parent comets and asteroids has been broadened even further by the action of P-R drag. Most of the Earth-crossing non-family asteroidal orbits have eccentricities of 0.1 or less.

The Eos, Themis and Koronis populations are modeled in a slightly different manner. For each family we generate a set of 1017 particles, each with the same distribution in semi-major axis, proper eccentricity and proper inclination as their respective families, but with randomly assigned proper longitudes of ascending node, proper arguments of pericenter and mean longitude. Each of these sets resembles a thin torus. To each of these sets of proper elements we vectorally add the forced elements of the asteroid families. We use the forced elements of the families at a point in the past such that after evolving the particle orbits they arrive at 1AU at the present time. For the particles we model in this chapter these times correspond to 52, 56 and 48 thousand years before present for the Eos, Themis and Koronis families respectively. The forced elements of the asteroid families at these times were found by integration backwards in time using the RADAU program. We then integrate forward in time the particle orbits with RADAU until each torus has evolved to become Earth-crossing. Figures 4-14 through 4-19 show the evolution of the dust particle orbits from these three families as the particles migrate from the asteroid belt into the inner Solar System. The circular structure of the distribution of orbital elements plotted in these figures is a unique characteristic of asteroid family members.

Figures 4–14 and 4–15 for the Eos particles demonstrate that the proper inclinations of the orbits are not affected by P-R drag. They also clearly show the decay of the proper eccentricity of the orbits due to P-R drag. Recall from Chapter 3 that the displacement of the distributions from the origin in $(I \cos \Omega, I \sin \Omega)$ and $(e \cos \tilde{\omega}, e \sin \tilde{\omega})$ space is a result of the forced elements at a particular semi-major axis and time. The radius of the circular distribution is an indication of the proper elements. Notice that as the orbits decay from about 3AU to 1AU the forced elements change. In the case of the eccentricities the circularization of the orbits by P-R drag has caused the eccentricities to cluster around the origin. For the Themis and Koronis particles shown in Figures 4–16 to 4–19 orbital scattering by Mars and the Earth disrupts the circular distribution of the inclinations. However, the proper eccentricities are still reduced by P-R drag.

Capture Rates

Using equation (3.43) we calculate the capture rates for the Earth-crossing orbits shown in the previous figures. In this chapter we use inclinations with respect to the J2000 ecliptic. This means that the inclination of the Earth's orbit is nearly equal to zero and therefore the latitude of the Earth in this frame, the variable β in equation (3.43), is also nearly equal to zero. Figure 4–20 shows the capture rates plotted against the geocentric encounter velocity of the particle *prior* to it being accelerated by the Earth's gravitational field. In Figure 4–20 the capture rates for the cometary orbits are designated by the crossed points, the Eos orbits are the open circles and the Themis and Koronis orbits are the filled circles. The average capture rate for the non-family asteroidal orbits was found to be $N/t = 150 \text{ Gyr}^{-1}$. For the purpose of reducing clutter only this average non-family asteroidal rate appears in Figure 4–20 (large crossed circle).

Due to their higher eccentricities the Earth-crossing cometary particles encounter the planet at substantially higher velocities than the asteroidal particles and therefore the effective capture cross-section of the Earth is smaller. Also, the higher eccentricities of the cometary particles result in a lower average spatial density compared with the asteroidal particles. These two factors, when combined, result in lower capture rates for cometary particles, as is apparent in Figure 4-20. Due to their higher inclinations the Earth-crossing Eos particles have capture rates similar to the average non-family asteroidal rate. However, the Earth-crossing Themis and Koronis particles typically have ecliptic inclinations less than 3 or 4 degrees, with some variation due to scattering by Mars and the Earth. The effective capture cross-section of the Earth for these Themis and Koronis particles is severely gravitationally enhanced, between 100-1000 times greater than that for cometary particles. The average spatial density of particles from Themis and Koronis is also higher than for particles from the other sources. The result is that capture rates for the low eccentricity, low inclination Themis and Koronis particles dominate the capture rates for particles from all other sources.

Contribution to the IDPs

From our two dust band models we estimate that the broad range of contributions listed in Table 2-1 (5% to 25%) is representative of the fraction of all particles *in the zodiacal cloud* due to asteroid families. In this section we use these estimates to represent the fraction of all particles *in the Earth-crossing population* due to asteroid families. Using these two estimates we combine the relative contributions from each family listed in Table 2-1 with the averages of the capture rates shown in Figure 4-20 in order to calculate the percentages of IDPs from each source.

If the fraction of all particles on Earth-crossing orbits from a given source is designated by n , then, from Table 2-1, the range for Earth-crossing Eos particles is $n_{eos} = 0.04$ to 0.21 and for Earth-crossing Themis and Koronis particles as $n_{tk} = 0.01$ to 0.04 . Then the fraction of all particles on Earth-crossing orbits from the three families ranges from $n_{eos} + n_{tk} = 0.05$ to 0.25 . Then let the number of IDPs deposited per unit time from a given source be designated by N and normalize to cometary IDPs such that $N_{com} \equiv 1$. We normalize the capture rates such that the average capture rate for cometary particles is $\bar{p}_{com} \equiv 1$. The number of Eos IDPs deposited for each cometary IDP is a product of the normalized average Eos capture rate and the ratio of the Earth-crossing Eos particles to the Earth-crossing cometary particles, or

$$N_{eos} = \bar{p}_{eos} \left(\frac{n_{eos}}{n_{com}} \right). \quad (4.2)$$

We rewrite this expression as

$$N_{eos} = \frac{n_{ast}}{n_{com}} \left[\bar{p}_{eos} \left(\frac{n_{eos}}{n_{ast}} \right) \right]. \quad (4.3)$$

Similarly, the number of Themis and Koronis IDPs deposited for each cometary IDP is given by

$$N_{tk} = \frac{n_{ast}}{n_{com}} \left[\bar{p}_{tk} \left(\frac{n_{tk}}{n_{ast}} \right) \right] \quad (4.4)$$

and, therefore, the number of the remaining non-family asteroidal IDPs deposited for each cometary IDP is

$$N_{nf} = \frac{n_{ast}}{n_{com}} \left[\bar{p}_{nf} \left(\frac{n_{ast} - n_{eos} - n_{tk}}{n_{ast}} \right) \right]. \quad (4.5)$$

We also express the number of cometary IDPs deposited per unit time (recall $\bar{p}_{com} \equiv 1$ and $N_{com} \equiv 1$) in the following manner

$$N_{com} = \frac{n_{ast}}{n_{com}} \left[\bar{p}_{com} \left(\frac{n_{com}}{n_{ast}} \right) \right]. \quad (4.6)$$

Table 4-1: Normalized average capture rates.

	Cometary	Non-family Asteroidal	Eos	Themis Koronis
\bar{p}	1	30	30	160

Summing equations (4.3) through (4.6) gives the total number of IDPs deposited per unit time from all sources for each cometary IDP deposited

$$N_{tot} = \frac{n_{ast}}{n_{com}} \left[\bar{p}_{eos} \left(\frac{n_{eos}}{n_{ast}} \right) + \bar{p}_{tk} \left(\frac{n_{tk}}{n_{ast}} \right) + \bar{p}_{nf} \left(\frac{n_{ast} - n_{eos} - n_{tk}}{n_{ast}} \right) + \bar{p}_{com} \left(\frac{n_{com}}{n_{ast}} \right) \right]. \quad (4.7)$$

By combining the normalized average capture rates of Table 4-1 with the contributions shown in Table 2-1 we are able to use equations (4.3) through (4.7) to determine the percentages of IDPs from each of our proposed sources. These ratios, N_{tk}/N_{tot} , N_{eos}/N_{tot} , N_{nf}/N_{tot} , and N_{com}/N_{tot} appear in Figure 4-21.

There is a great deal of controversy concerning the relative contributions of comets and asteroids to the zodiacal cloud. We do not wish to add to this controversy at this time. A wide range of estimates representing the cometary contribution to the zodiacal cloud can be accommodated by Figure 4-21. The plot on the left of Figure 4-21 is for the case where 25% of all particles on Earth-crossing orbits are from the Eos, Themis and Koronis families. Earth-crossing cometary particles can then range from 0% to 75%, with the compliment (75% to 0%) being due to other asteroidal particles. The plot on the right of Figure 4-21 is for the case where 5% of all particles on Earth-crossing orbits are from the Eos, Themis and Koronis families. In this case cometary particles could possibly account for 0% to 95% of the Earth-crossing population with the compliment (95% to 0%) from other asteroids. As an example, it has been suggested that the ratio

of dust production by asteroid families to dust production by all asteroids is about 1:3 (Durda and Dermott 1996). In this example, if dust from asteroid families contributes 25% to the Earth-crossing population (left plot of Figure 4-21) then all asteroids (non-family and family) contribute 75%. This leaves 25% to be supplied by comets. In Figure 4-21 on the left plot with cometary dust as 25% of the zodiacal cloud we see that Eos contributes about 20% to the IDPs, Themis and Koronis combine to provide another 20% and nearly all of the remaining IDPs are due to non-family asteroids. In this example cometary particles represent only about 2% of all IDPs.

From Figure 4-21 certain conclusions are almost unavoidable, regardless of the cometary contribution to the zodiacal cloud. The existence of the dust bands and the evidence that asteroidal dust is transported to the inner Solar System implies that most IDPs are asteroidal. Also, Figure 4-21 shows that even though the Themis and Koronis families may contribute only between 1% and 4% to the zodiacal cloud, these two families can make a very significant contribution to the population of IDPs. What may be most striking from Figure 4-21 is that under no circumstances does cometary dust represent more than 28% of the IDPs. An estimate based on Figure 4-21 and using a mean value between 5% and 25% dust from families is that probably fewer than 10% of IDPs are cometary. Losses due to melting and vaporization during atmospheric entry of the higher velocity cometary particles will further reduce their contribution to collections of intact IDPs retrieved from the stratosphere. The conclusions are clear, the Earth predominantly accretes asteroidal dust, and a large – perhaps dominant – fraction of this dust comes from the three asteroid families Eos, Themis and Koronis. Samples of these known S-type (Eos, Koronis) and C-type (Themis) asteroids may already exist in our IDP collections.

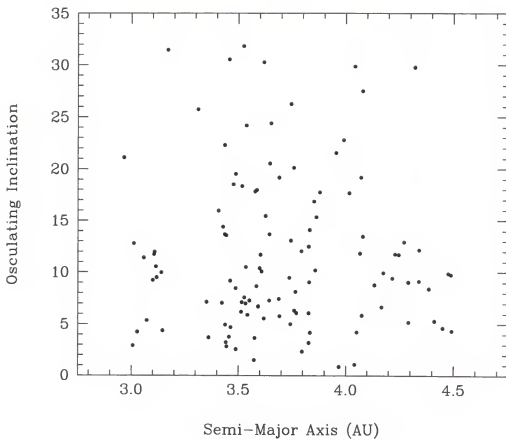


Figure 4-1: Distribution of osculating inclination verses semi-major axis for 118 short period Jupiter family comets.

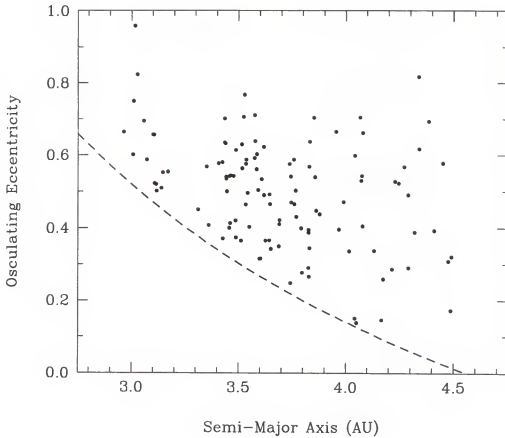


Figure 4-2: Distribution of osculating eccentricity verses semi-major axis for 118 short period Jupiter family comets. The dashed line marks the extreme limit of the Jupiter-crossing regime, using a semi-major axis and eccentricity of $a = 5.203$, $e = 0.062$ for Jovian orbit. These give a perihelion of $q = 4.88$ AU, which we further reduce by subtracting the sphere of action of the planet, $D_a \simeq 0.365$ AU.

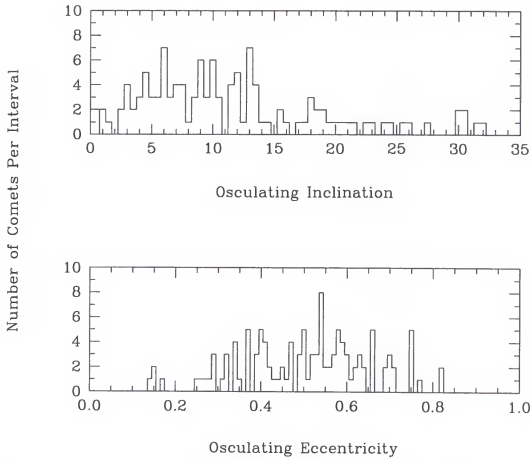


Figure 4-3: Histograms showing the inclination and eccentricity distributions of the comets plotted in Figures 4-1 and 4-2.

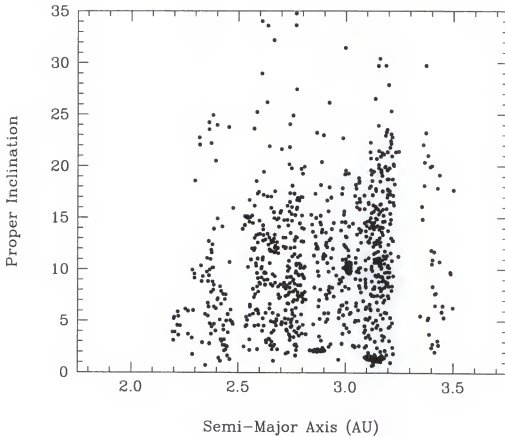


Figure 4-4: Distribution of proper inclination verses semi-major axis for all asteroids with absolute magnitude $H < 11$ (1053 asteroids). This plot is shown on the same scale as Figure 4-1 (with a shift of 1AU in semi-major axis) and shows that the Jupiter family of comets span the same range of inclination as the asteroids in the main belt. The asteroid family Eos is the cluster at approximately 3AU and 10° inclination. The Koronis and Themis families are the low inclination clusters to the left and right of 3AU, respectively. Notice that the Eos and Themis families have a higher dispersion in proper inclination than the Koronis family.

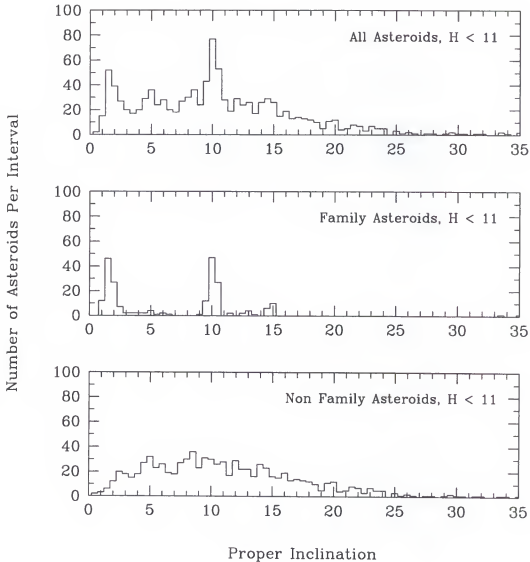


Figure 4-5: The top plot is a histogram of the all the asteroids shown in Figure 4-4. The middle plot shows only those asteroids of Figure 4-4 that are associated with families. The bottom plot is all the remaining background asteroids that are not associated with families. The families Themis and Koronis appear together at the feature inside of 3° proper inclination, Eos is at 10° and the next largest family Maria is at 15° . Several small families are also visible. From this plot we see that a large majority of the low inclination asteroids belong to the Themis and Koronis families and that more than half of the asteroids at 10° belong to the Eos family.

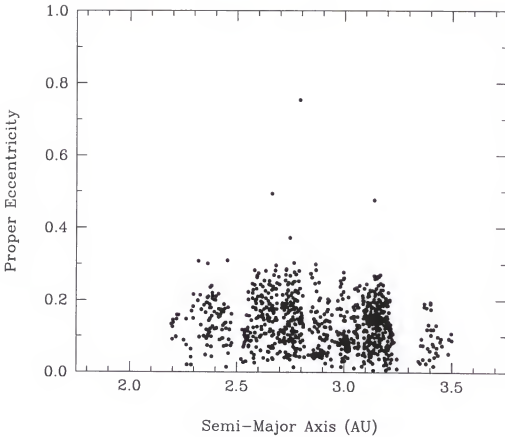


Figure 4-6: Distribution of proper eccentricity verses semi-major axis for all asteroids with absolute magnitude $H < 11$ (1053 asteroids). This plot, which is shown on the same scale as Figure 4-2 (with a shift of 1AU in semi-major axis), reveals the primary difference between the Jupiter family cometary population and the asteroidal population. The comets have much higher eccentricities. The asteroid families Eos and Koronis are apparent at 3AU, and just inside of 3AU respectively. The Themis family is slightly more difficult to discern here than in Figure 4-4, lying between 3.1 and 3.2 AU at about 0.15 in proper eccentricity.

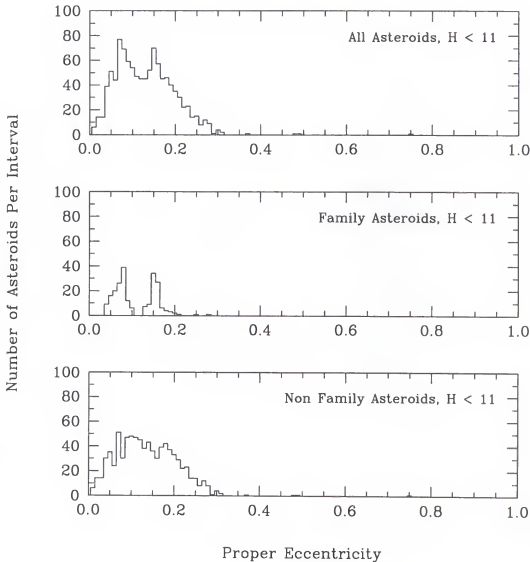


Figure 4-7: The top plot is a histogram of the all the asteroids shown in Figure 4-6. The middle plot shows only those asteroids of Figure 4-6 that are associated with families. The bottom plot is all the remaining background asteroids that are not associated with families.

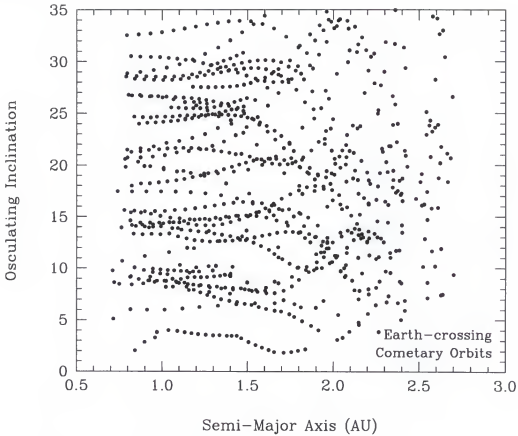


Figure 4-8: Distribution of osculating inclination verses semi-major axis for Earth-crossing orbits of cometary dust particles. The obvious tracking is due to the continuing evolution of particles from a single comet.

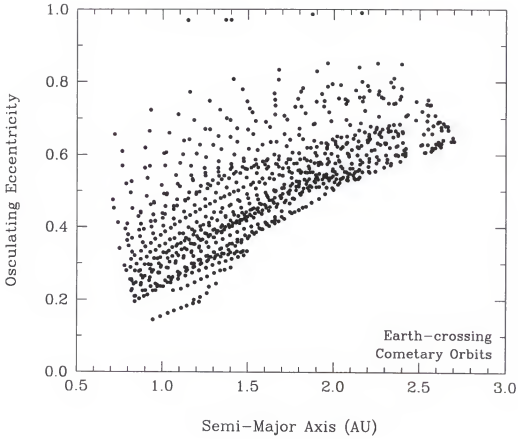


Figure 4-9: Distribution of osculating eccentricity verses semi-major axis for Earth-crossing orbits of cometary dust particles. The obvious tracking is due to the continuing evolution of particles from a single comet.

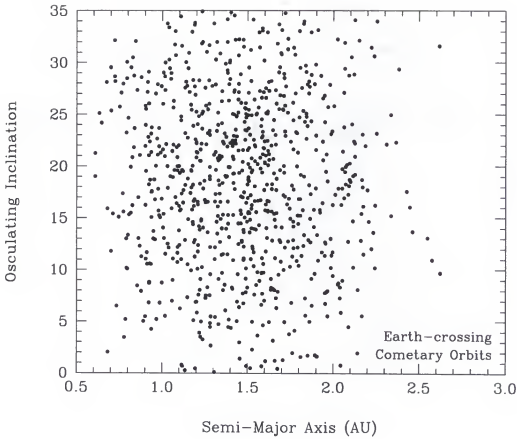


Figure 4-10: Smoothed distribution of osculating inclination verses semi-major axis for Earth-crossing orbits of cometary dust particles. We use the mean and dispersion of the orbital elements shown in Figure 4-8 to generate a random gaussian distribution of Earth-crossing cometary orbits.

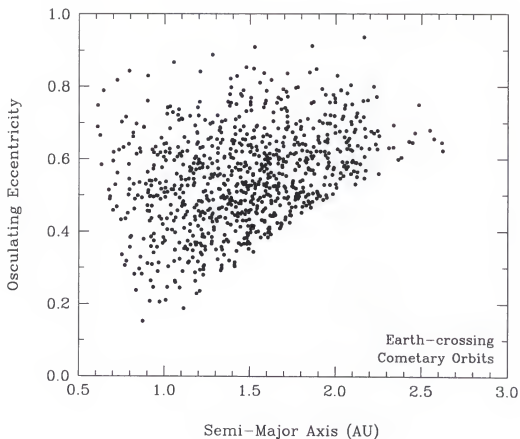


Figure 4-11: Smoothed distribution of osculating eccentricity versus semi-major axis for Earth-crossing orbits of cometary dust particles. We use the mean and dispersion of the orbital elements shown in Figure 4-9 to generate a random gaussian distribution of Earth-crossing cometary orbits.

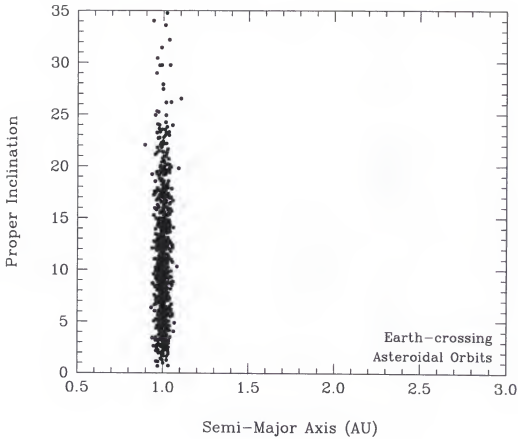


Figure 4-12: Distribution of proper inclination versus semi-major axis for Earth-crossing orbits of non-family asteroidal particles. This plot is shown on the same scale as Figure 4-10 and shows that the Earth-crossing cometary population spans the same range of inclination as the Earth-crossing asteroidal population.

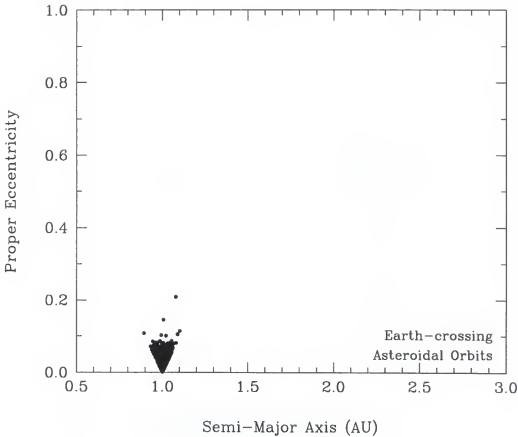


Figure 4-13: Distribution of proper eccentricity verses semi-major axis for Earth-crossing orbits of non-family asteroidal particles. This plot, which is shown on the same scale as Figure 4-11 reveals the primary difference between the Earth-crossing cometary population and the Earth-crossing asteroidal population. The cometary orbits have much higher eccentricities. As we will see, this leads to substantially higher geocentric encounter velocities for cometary particles than for asteroidal particles.

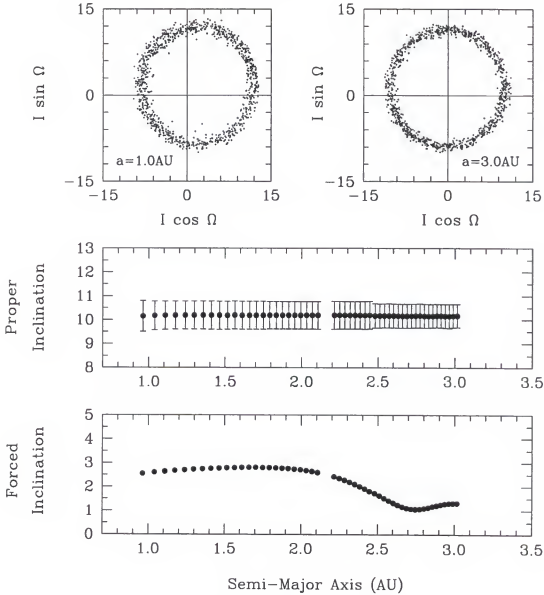


Figure 4-14: The orbital evolution of a wave of 10 micron diameter dust particles from the Eos family as their orbits decay from the asteroid family at 3AU into the inner Solar System. The middle plot tracks the evolution of the proper inclination and dispersion in proper inclination of the particles as their semi-major axes decay due to P-R drag. The displacement from the origin of the distributions in the upper two plots is due to the forced inclination, which is shown in the lower plot.

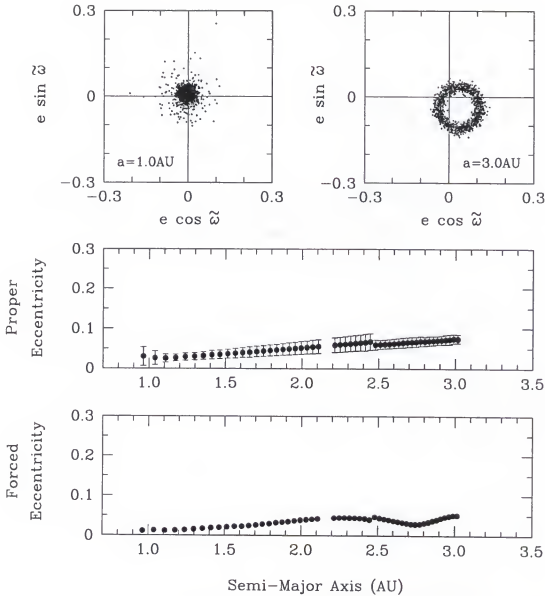


Figure 4-15: The orbital evolution of a wave of 10 micron diameter dust particles from the Eos family as their orbits decay from the asteroid family at 3AU into the inner Solar System. The middle plot tracks the evolution of the proper eccentricity and dispersion in proper eccentricity of the particles as their semi-major axes decay due to P-R drag. P-R drag also acts to reduce the proper eccentricity of the particles as their orbits decay towards the Sun. The displacement from the origin of the distributions in the upper two plots is due to the forced eccentricity, which is shown in the lower plot. At 1AU the distribution is nearly centered on the origin, indicating a very small forced eccentricity.

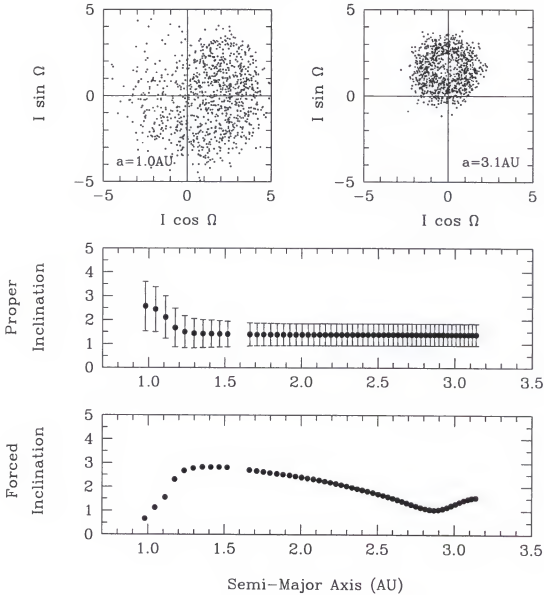


Figure 4-16: The orbital evolution of a wave of 10 micron diameter dust particles from the Themis family as their orbits decay from the asteroid family at 3.1 AU into the inner Solar System. The middle plot tracks the evolution of the proper inclination and dispersion in proper inclination of the particles as their semi-major axes decay due to P-R drag. The displacement from the origin of the distributions in the upper two plots is due to the forced inclination, which is shown in the lower plot.

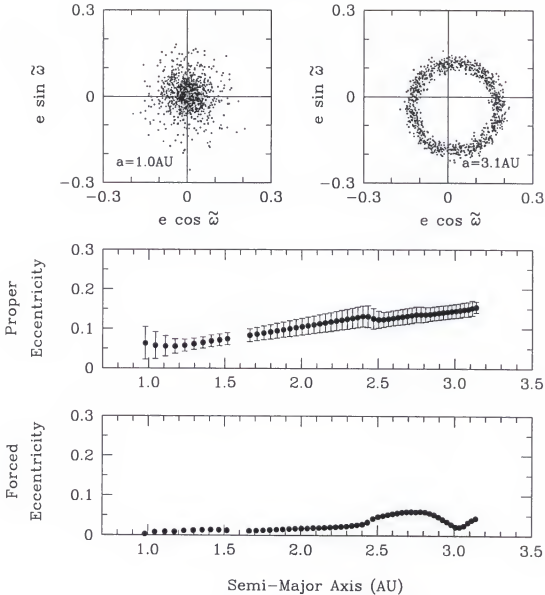


Figure 4-17: The orbital evolution of a wave of 10 micron diameter dust particles from the Themis family as their orbits decay from the asteroid family at 3.1 AU into the inner Solar System. The middle plot tracks the evolution of the proper eccentricity and dispersion in proper eccentricity of the particles as their semi-major axes decay due to P-R drag. P-R drag also acts to reduce the proper eccentricity of the particles as their orbits decay towards the Sun. The displacement from the origin of the distributions in the upper two plots is due to the forced eccentricity, which is shown in the lower plot. At 1AU the distribution is nearly centered on the origin, indicating a very small forced eccentricity.

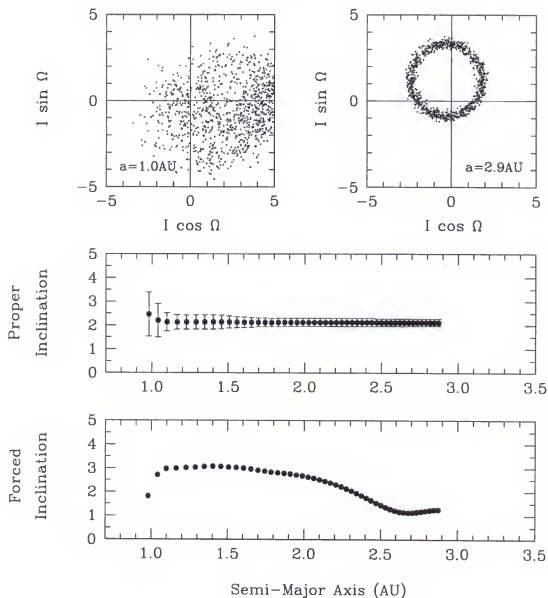


Figure 4-18: The orbital evolution of a wave of 10 micron diameter dust particles from the Koronis family as their orbits decay from the asteroid family at 2.9 AU into the inner Solar System. The middle plot tracks the evolution of the proper inclination and dispersion in proper inclination of the particles as their semi-major axes decay due to P-R drag. The displacement from the origin of the distributions in the upper two plots is due to the forced inclination, which is shown in the lower plot.

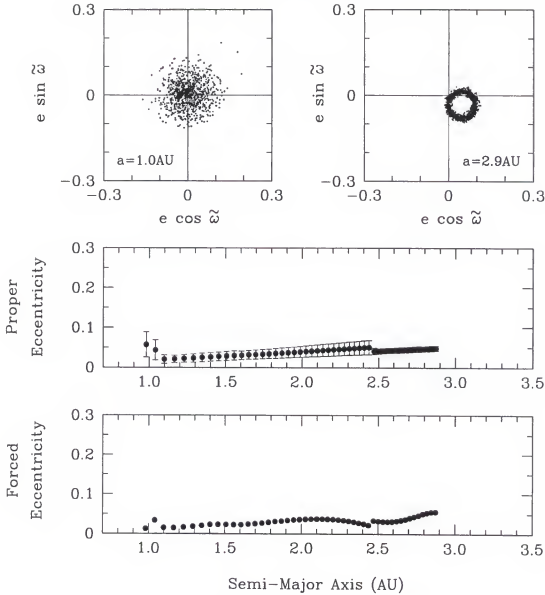


Figure 4-19: The orbital evolution of a wave of 10 micron diameter dust particles from the Koronis family as their orbits decay from the asteroid family at 2.9 AU into the inner Solar System. The middle plot tracks the evolution of the proper eccentricity and dispersion in proper eccentricity of the particles as their semi-major axes decay due to P-R drag. P-R drag also acts to reduce the proper eccentricity of the particles as their orbits decay towards the Sun. The displacement from the origin of the distributions in the upper two plots is due to the forced eccentricity, which is shown in the lower plot. At 1AU the distribution is nearly centered on the origin, indicating a very small forced eccentricity.

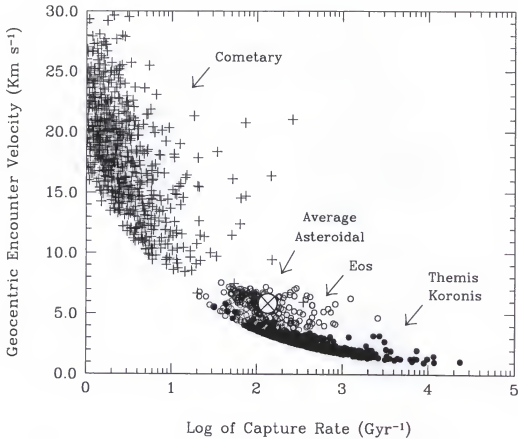
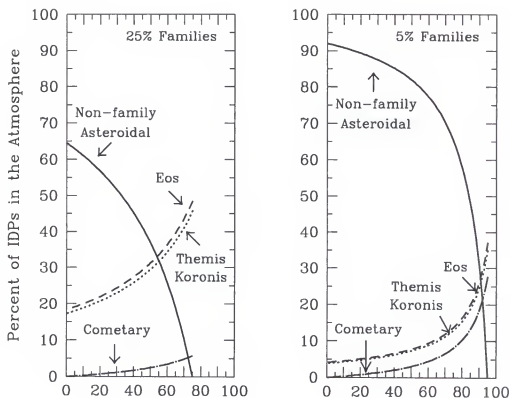


Figure 4-20: Capture rates for dust particles on the Earth-crossing orbits shown in Figures 4-10 through 4-19 are plotted against the geocentric encounter velocity of the particles. This is the velocity of the particles prior to being accelerated by the Earth's gravitational field. The average capture rate for non-family asteroidal particles is designated by the large crossed circle at 150 Gyr⁻¹ and 6 km s⁻¹. Cometary capture rates are the crossed points, Eos rates the open circles and Themis and Koronis rates the filled circles.



Cometary Dust as Percent of Earth-Crossing Population

Figure 4-21: Percentages of IDPs in the atmosphere are determined by combining the data of Figure 4-20 with the information shown in Table 2-1.

CHAPTER 5

VARIATIONS IN THE RATE OF ACCRETION

Muller and MacDonald (1995) suggested that the rate of accretion of IDPs might vary with the changing inclination of the Earth's orbit and that these variations might drive the Earth's 100,000 year climate cycle. Farley and Patterson (1995) have taken measurements of extraterrestrial ^3He concentrations and $^3\text{He}/^4\text{He}$ ratios in a deep-sea sediment core for the period spanning 250,000 to 450,000 years ago. These measurements show that the flux of IDPs to the sea floor has varied by a factor of 2 to 3 with a period near 100,000 years. Farley and Patterson interpret these variations as indicative of a variable dust accretion rate that seems to be correlated with either the varying eccentricity of the Earth's orbit or the varying inclination of the Earth's orbit, or both. Recently, however, Marcantonio *et al.* (1996) have measured concentrations of extraterrestrial ^3He and terrestrial ^{230}Th in deep-sea sediments dating back 250,000 years. They find the variations in the ^3He abundances to be highly correlated with variations in the ^{230}Th abundances. They also find these variations to be related to the Earth's climate record and suggest that the cause is climate driven changes in deep ocean currents. Using the $^3\text{He}/^{230}\text{Th}$ ratio Marcantonio *et al.* suggest that the accretion rate of the ^3He bearing IDPs probably does not vary by more than 73%. They also *do not* find a 100,000 year periodicity in the accretion rate.

In this chapter we investigate possible mechanisms that may cause variations in the accretion rate of dust particles from the Eos, Themis and Koronis asteroid families. We model three sizes of particles for which the ratio of radiation pressure to gravitational force, β_f , is 0.638, 0.0469 and 0.0235. For spherical dust particles composed of

“astronomical silicate” (Drain and Lee 1984) and having a density of 2.5 g cm^{-3} these β_f values correspond to diameters of 1, 10 and 20 microns respectively. There is still debate as to origin of the ^3He in IDPs, whether it is implanted solar helium or trapped primordial gas. Modeling of atmospheric entry heating of IDPs shows that in either case IDPs in the limited size range 7–20 microns diameter will be responsible for transporting most of the ^3He to the sea floor (Farley *et al.* 1996).

Initial Conditions

To evaluate the hypothesis of a variable dust accretion rate it is necessary to first recognize that we should be using the inclination of the Earth’s orbit with respect to the plane of symmetry of the dust band material at 1AU, not with respect to the invariable plane of the Solar System, as has been suggested by Muller and McDonald (1995) and Farley and Patterson (1995). In order to reconstruct the historical orientation of the dust bands with respect to the Earth’s orbit it is necessary to know the orbital elements of the planets and of the asteroid families back in time. We attempted to obtain these elements by using the RADAU program to integrate seven planets and the members of the three asteroid families back 1.2 million years. As a check of the accuracy of this method we compare the orbital elements of the Earth obtained from RADAU with the orbital elements from Quinn *et al.* (1991). Figure 5–1 compares the orbital inclination and ascending node for the Earth obtained from RADAU and from Quinn *et al.* dating back 1.2 million years and referred to the J2000 ecliptic and mean equinox. After less than 100,000 years the two sets begin to diverge. After 400,000 years the inclinations differ by half a degree or more and the ascending nodes swing 180 degrees out of phase. Quinn *et al.* state that after three million years of integration of the entire Solar System (nine planets) they have obtained the ecliptic longitude of the Earth to an accuracy of

0.03 radians. This is an accuracy in the position of the Earth of about 1.75 days after 3 million years. They report that the largest error in the orbital elements of the Earth are not greater than 4 parts in 10^6 after 3 million years. Due to the apparent inaccuracy of our data obtained from the RADAU program for integrations lasting longer than about 100,000 years we use the planetary orbital elements from Quinn *et al.* to establish our initial conditions.

Figure 5–2 compares the orbital inclination and ascending node for Jupiter from Quinn *et al.* and obtained from RADAU during the same integration as shown in Figure 5–1. In the case of the more massive Jupiter both data sets agree, with the only observable differences coming after about one million years. Figure 5–3 shows the results from integrating the Eos, Themis and Koronis asteroid families along with seven planets back 1 million years using RADAU. The forced inclinations and forced ascending nodes of the families are plotted together with the inclination and node of Jupiter. The forced elements of these families are locked onto the orbit of Jupiter. Since we know that RADAU can accurately integrate the orbit of Jupiter back at least 1.2 million years, and these families are locked onto Jupiter, we can continue using RADAU to accurately integrate these small bodies in the asteroid belt in order to set up our initial conditions. For the largest particles considered by us the orbital decay from the asteroid belt to 1AU requires about 100,000 years, so we can continue to use RADAU for each of the individual integration runs that bring the asteroidal particles from the main-belt to the inner Solar System.

Generation and Evolution of Dust Particle Orbits

We choose a time interval of 20,000 years, about equal to the interval in the ^3He record. We use the members of the asteroid family Eos to determine the forced elements of dust particles at 1AU. Using RADAU we integrate the orbits of particles from the Eos

family, releasing a wave of 249 particles from the family every 20,000 years and letting their orbits decay under P-R drag and solar wind drag into the inner Solar System. For the extended variations dating back 1.2 million years we model particles of diameter 1 and 10 microns. For the shorter period of the ^3He record, spanning 250,000 to 450,000 years ago, we also model particles with diameters of 20 microns. We track the proper inclination and proper eccentricity of these migrating waves of Eos particles. When they become Earth-crossing we determine the forced inclination and the forced ascending node of the distribution with respect to the J2000 ecliptic and mean equinox. To clarify, the proper inclination of a dust band indicates the angular thickness of the dust band. For instance, the Eos dust band is composed of particles with proper inclinations of about 10° so the angular thickness of the Eos dust band is about 20° ($\pm 10^\circ$ from the plane of symmetry). The forced inclination of a dust band indicates the tilt of the plane of symmetry of the dust band with respect to a designated reference plane. At this point we do away with the fixed J2000 ecliptic as a reference plane and introduce the term "mutual inclination" to refer to the inclination between any two varying orbital planes. For example, in Figure 5-4 the solid line is the mutual inclination between the varying orbit of the Earth and the varying orbit of Jupiter. Notice that in this Jovian reference frame the inclination of the Earth's orbit varies with roughly a 100,000 year periodicity whereas in the J2000 ecliptic reference frame the variation has roughly a 70,000 year periodicity (See Figure 5-1). Recall from Figure 5-3 that in the asteroid belt the forced inclinations of the three asteroid families are locked onto the orbit of Jupiter, so their plane of symmetry in the belt is in fact the plane of Jupiter's orbit, not the invariable plane. Therefore the solid line in Figure 5-4 represents the initial conditions of the particles in the asteroid belt. Figure 5-4 also shows the mutual inclination between the varying orbit of the Earth and the plane of symmetry of the Eos dust particles when they

are at 1AU. The mutual inclination is plotted for both 1 and 10 micron diameter particles. The smallest 1 micron diameter particles essentially maintain their initial conditions after being transported to 1AU. The larger particles however have different forced inclinations at 1AU than their initial conditions in the asteroid belt. This is a consequence of the time required under P-R drag for the particle orbits to decay to 1AU from the asteroid belt. The small 1 micron diameter particles require about 3700 years to reach 1AU. The larger 10 micron diameter particles require about 50,000 years to reach 1AU from the asteroid belt. Several things happen to these larger particles with more slowly decaying orbits. Secular perturbations from the planets varying with a period comparable to this orbital decay time cause changes in the forced elements of the distribution as it decays from the asteroid belt to 1AU. The particles pass by the secular resonances at the inner edge of the belt more slowly and so their orbits are more scattered. They also pass by Mars more slowly and approach the Earth more slowly. All of these factors influence the forced elements and dispersions of the proper elements of the large particle orbits more than the small particle orbits.

Because the small 1 micron diameter particles reach 1AU with nearly the same forced inclination with respect to the Earth's orbit as they initially had in the asteroid belt, we use the varying mutual inclination between the Earth's orbit and Jupiter's orbit to represent the varying forced inclination at 1AU for small particles. We feel this is justified because: (1) the forced elements of the asteroid families are locked onto Jupiter's orbit; (2) our runs for 1 micron diameter particles shows that they reach 1AU with little change in their forced elements. By doing this the resolution is increased from one point every 20,000 years to one point every 492 years, which is the resolution of the data set obtained from Quinn *et al.*

Table 5-1: Proper elements and dispersions for 1 micron diameter particles at 1AU.

	Eos	Themis	Koronis
$I_p \pm \delta I_p$	$10.^{\circ}2 \pm 0.5$	$1.^{\circ}4 \pm 0.6$	$2.^{\circ}1 \pm 0.4$
$e_p \pm \delta e_p$	0.04 ± 0.01	0.05 ± 0.03	0.03 ± 0.02

Figures 5-5 and 5-6 give a demonstration of the orbital evolution of a wave of 1 micron diameter Eos particles originating in the asteroid belt and ending at 1AU. For these small particles on quickly decaying orbits the proper inclination of the distribution is not dramatically dispersed and the forced elements are nearly constant. The effect of P-R drag on the proper eccentricities is clearly evident. Also, passage through resonant regions in the asteroid belt at about 2.8AU and at about 2.4AU produces noticeable changes in the proper and forced eccentricities. Figures 5-7 through 5-10 demonstrate the evolution of 1 micron diameter particles from the Themis and Koronis families. These six figures give us the proper elements and proper element dispersions that are used in the calculation of the varying capture rates for small 1 micron diameter particles. These proper elements and dispersions are listed in Table 5-1.

We have also modeled the orientation of dust bands made of 10 micron diameter particles back 1.2 million years. Figure 5-4 shows that the forced plane of symmetry of the 10 micron diameter particles at 1AU has changed dramatically from the initial conditions in the asteroid belt. Therefore, we must use the actual results from the integration runs performed every 20,000 years and so the resolution of our 10 micron diameter variations drops by a factor of 40 compared with the 1 micron resolution. Figures 4-14 through 4-19 in the previous chapter give us the proper elements and dispersions for 10 micron diameter particles from the three families at 1AU. These proper elements

Table 5-2: Proper elements and dispersions for 10 micron diameter particles at 1AU.

	Eos	Themis	Koronis
$I_p \pm \delta I_p$	$10.^{\circ}2 \pm 0.6$	$2.^{\circ}6 \pm 1.1$	$2.^{\circ}5 \pm 0.9$
$e_p \pm \delta e_p$	0.03 ± 0.02	0.06 ± 0.04	0.06 ± 0.04

are listed in Table 5-2. Gravitational scattering by Mars and the Earth and resonant trapping by the Earth of these slower moving particles disperses their orbits to somewhat higher proper inclinations and eccentricities compared to the 1 micron diameter particles. The forced eccentricities for both the 1 and 10 micron diameter particles is set to zero for the variations modeled here.

Variable Capture Rates

Method of the Moving Torus

At each point in the data set of the mutual inclination (every 492 years for small particles and every 20,000 years for larger particles) a torus of particle orbits having the proper elements and dispersions of a particular family is passed by the Earth. We begin at the outer limit of Earth-crossing orbits where the perihelion of the particle orbits is just inside of the aphelion of the Earth's orbit. We conclude in the opposite sense, with the aphelion of particle orbits just outside of the perihelion of the Earth's orbit. For each step in semi-major axis of this torus we revolve the Earth once in its orbit, sampling the capture rate as given by equation (3.43) at one day increments (roughly one degree in longitude). For each of these 360 discrete positions of the Earth in its orbit a random gaussian distribution in proper eccentricity consisting of 30 orbits is generated using the elements listed in Tables 5-1 or 5-2. For each of these 30 orbital eccentricities a random gaussian distribution in proper inclination for an additional 30 orbits is generated using

the elements in Tables 5-1 or 5-2. If the latitude of the Earth with respect to the plane of symmetry of the dust band is greater than the proper inclination of a particular orbit then the capture rate of particles on that orbit, at that particular latitude of the Earth, is set to zero. The capture rates for a complete revolution of the Earth in its orbit are averaged, the semi-major axis of the torus is decreased by one increment and the procedure is repeated. The increment in semi-major axis is determined by the eccentricity of the Earth and of the particles and is adjusted at each time step such that there are 30 equal steps in semi-major axis for the torus. For each time step (every 492 or 20,000 years) this results in a population of 9,720,000 Earth-crossing orbits. The mean capture rate for these orbits is calculated, producing an average capture rate over the course of one year. This yearly average capture rate is plotted as a single point on the plots showing variations in this chapter.

Demonstration of the Method

Figure 5-11 is an example of the variations that would result if the mutual inclination between the varying orbit of the Earth and the plane of symmetry of a dust band varied as a sine wave with period of 100,000 years. The dashed line represents the proper inclination of 1 micron diameter Themis particles at 1AU (From Table 5-1). The base line of the varying mutual inclination has been set equal to the proper inclination and the amplitude is one degree. When the mutual inclination is greater than the proper inclination of the dust band the Earth is not completely embedded in the dust band but instead passes through twice each year, as is shown in the schematic representations in Figure 5-12. The plots of the test sine wave in Figure 5-11 allow us to identify two competing processes in the varying capture rate. When the Earth is embedded in the dust band, with the mutual inclination below the dashed line in the plot, the capture rate is at a maximum. Evidence of the changing eccentricity of the Earth's orbit is visible in the peaks of the capture

rate, which appear at points to have been "lopped off" due to the increasing eccentricity. This is a result of the varying geocentric encounter velocity, which increases when the eccentricity of the Earth increases, resulting in a smaller effective cross-section. The dominant process however is due to the changing mutual inclination. When the Earth is not embedded within the dust band the averaged capture rate decreases.

Variations for Small Particles

Figure 5-13 shows the variations in the capture rate that result from the real changes in the mutual inclination between the Earth's orbit and the plane of symmetry of 1 micron diameter dust bands at 1AU. In Figure 5-13 we model 1 micron diameter Themis particles using the proper elements listed in Table 5-1. Figure 5-14 shows the variations in the capture rate for 1 micron diameter Koronis particles. Due to the two distinct proper inclinations of the Themis and Koronis particles the variations in the capture rates differ. First, because of the higher proper inclination of the Koronis particles the mutual inclination does not exceed the proper inclination by as much as in the case for Themis particles. The result is that the Earth spends more time embedded in the Koronis dust band than in the Themis dust band. This is especially true for the first 600,000 years of the variations. The result is that the variations in the capture rate for the Koronis dust band are not as extreme as the variations in the capture rate for the Themis dust band. Also, because of the higher proper inclination the geocentric encounter velocity of the Koronis particles is slightly higher than the Themis particles, resulting in a smaller effective cross-section. Finally, the higher proper inclination and slightly smaller dispersion in proper inclination of the 1 micron diameter Koronis particles leads to a different average spatial density compared to the Themis particles. This leads to slightly lower average capture rates and noticeable spikes in the capture rate when the mutual inclination passes through the edges of the dust band. These spikes are due to the enhanced spatial density near the

extremes in latitude of the dust band material. Similar spikes do not exist in the Themis capture rates because the dispersion in proper inclination for these particles is higher, giving the dust band the appearance of a thin sheet more than a banded structure.

Figure 5-15 shows the capture rate variations for 1 micron diameter Eos particles using the proper elements listed in Table 5-1. The large 10° proper inclination of the Eos particles assures that the Earth is always embedded within this dust band. However, the varying eccentricity of the Earth's orbit still causes changes in the capture rate. Because of the high proper inclination the capture rates of these Eos particles is about 5 to 10 times lower than the rates for the Themis and Koronis particles. The effect of the varying mutual inclination is virtually absent from the capture rate and only the variation due to the Earth's eccentricity remains. The maximum values of the capture rate occur at minimums in the Earth's eccentricity. Since Eos particles have a proper inclination about equal to the mean for the asteroid belt we expect that any variation in the accretion of non-family main-belt asteroidal particles will follow the variations shown here.

Variations for Large Particles

The 10 micron diameter particles take approximately 10 times longer than 1 micron particles to reach 1AU from their source. Planetary perturbations over this longer time span change the forced elements of these particles (See Figures 4-14 through 4-19). Figure 5-4 shows that at 1AU the mutual inclination between the orbit of the Earth and the forced plane of symmetry of the 10 micron particles is different than the mutual inclination in the source region. Therefore, for the capture rates of these 10 micron particles we must use our lower resolution of 20,000 years. From Table 5-2 we see that for the 10 micron diameter particles the Themis and Koronis distributions are nearly identical. Because of this similarity we model variations in the capture rate for particles from both families

together. Figure 5-16 shows these variations. Because of the higher proper inclination the mutual inclination seldom rises above the proper inclination. Even in the few instances when the mutual inclination is high, the large dispersion in proper inclination insures that the Earth is almost always embedded in the dust band material. Because of this the variations in the capture rate are small and in fact show more correlation with the varying eccentricity of the Earth's orbit than with the mutual inclination. However, the average capture rate for these 10 micron particles is about the same as that for the smaller particles.

Because of their higher proper inclinations the Eos particles do not suffer from as much scattering due to planetary perturbations. Comparing Tables 5-1 and 5-2 we see that the proper element distributions for the 10 micron diameter Eos particles nearly matches the 1 micron distribution. In fact the proper eccentricity is slightly lower for the 10 micron Eos particles, though also slightly more dispersed. Figure 5-17 shows the variations in the capture rate of 10 micron diameter Eos particles using the proper elements listed in Table 5-2. As was the case for the 1 micron Eos capture rates, there is no sign of a variation due to the varying mutual inclination but there is a strong correlation with the varying eccentricity of the Earth's orbit.

The variation in the capture rate of both the large and small Eos particles is linked to the varying eccentricity and not the varying mutual inclination. Since the Eos asteroid family has a proper inclination about equal to the mean for the asteroid belt we expect that any variation in the accretion of non-family main-belt asteroidal particles will also be correlated with the varying eccentricity of the Earth's orbit and therefore should be independent of the forced mutual inclination at 1AU (ie., independent of particle size).

Comparison With Other Records

The Periodic ^3He Record

Marcantonio *et al.* (1996) show that variations in ^3He abundances in deep-sea sediments may not be due to variations in accretion of IDPs. In spite of this, or perhaps in support these findings, we include comparisons of our predicted accretion rate variations with the ^3He flux data of Farley and Patterson (1995). For this shorter time span of 250,000 to 450,000 years we modeled variations for 20 micron diameter particles as well, using the same techniques as used for the 10 micron diameter particles. Figure 5-18 shows the ^3He variations plotted with our accretion rates for 1, 10 and 20 micron diameter Themis and Koronis particles (only Themis 1 micron are shown in the plot). The ^3He is believed to be deposited by dust particles between 7 and 20 microns diameter. Only the variation in the accretion rate for 1 micron diameter Themis particles has an amplitude and period comparable with the ^3He flux data, however, the two curves are not in phase. The much smaller variations of the 10 and 20 micron accretion rates are also out of phase with the ^3He data. Figure 5-19 shows the ^3He variations plotted with our accretion rates for 1, 10 and 20 micron diameter Eos particles. These accretion rates vary primarily due to the varying eccentricity of the Earth's orbit, and they too are out of phase with the ^3He data. We find no variations which support the ^3He record. We also do not expect significant changes in the variations for larger size particles.

The Climate Record

Possible connections between a periodic variation in the accretion rate of interplanetary dust and the Earth's climate record have recently been suggested (Muller and MacDonald 1995; Farley and Patterson 1995). Figure 5-20 compares our variation in the capture rate of 1 micron diameter Themis particles with the climate record for the

last 1.2 million years. The climate record is from Imbrie *et al.* (1993) after removal of the well understood shorter period Milankovitch frequencies, which are well understood. The cause of the remaining 100,000 year climate cycle shown in the plot, by far the most dominant cycle for the last 800,000 to 1 million years, is unknown. Our analysis of the data in Figure 5-20 is limited to an "eyeball" study of the phase of the two curves and crude segmented power spectrums of each. There are some rather curious similarities. Note that for both the capture rate and climate record the 100,000 year periodicity nearly vanishes from the 0-600 ka interval to the 600-1200 ka interval. However, there are also apparently damning conflicts, especially at 650,000 years ago.

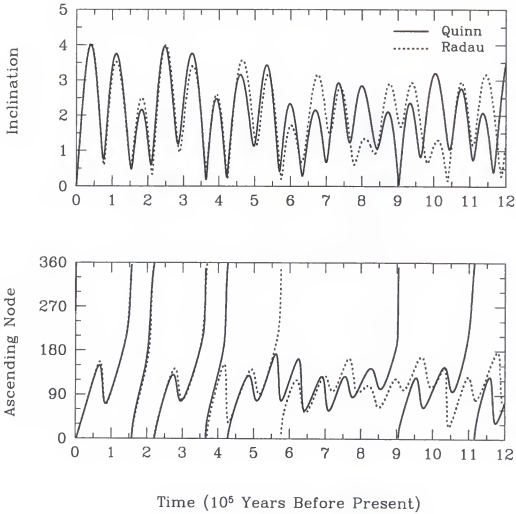


Figure 5-1: Comparison of the inclination and longitude of ascending node of the Earth's orbit determined by backwards integration of the Solar System with the RADAU integrator (dashed lines – Mercury and Pluto excluded) and from Quinn *et al.* (1991; solid lines – all planets included). These orbital elements are with respect to the J2000 ecliptic and mean equinox. Quinn *et al.* report that the largest error in their calculated orbital elements of the Earth is not greater than 4 parts in 10^6 after 3 million years of integration. After less than 100,000 years of integration there are noticeable differences between the two curves.

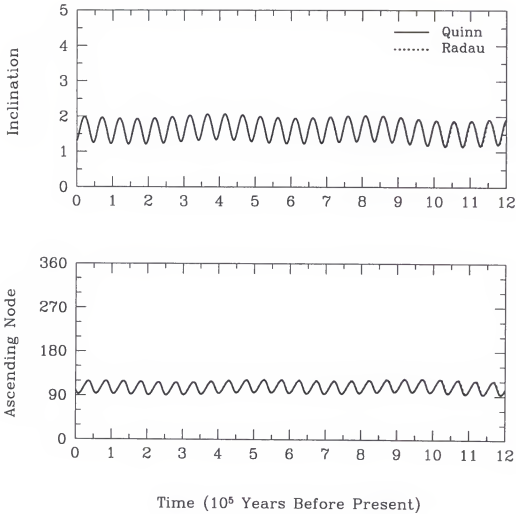


Figure 5-2: Comparison of the inclination and longitude of ascending node of Jupiter's orbit determined by backwards integration of the Solar System with the RADAU integrator (dashed lines – Mercury and Pluto excluded) and from Quinn *et al.* (solid lines – all planets included). These orbital elements are with respect to the J2000 ecliptic and mean equinox. The orbits of the more massive Jovian planets are more stable than the orbit of the Earth in the RADAU integrator.

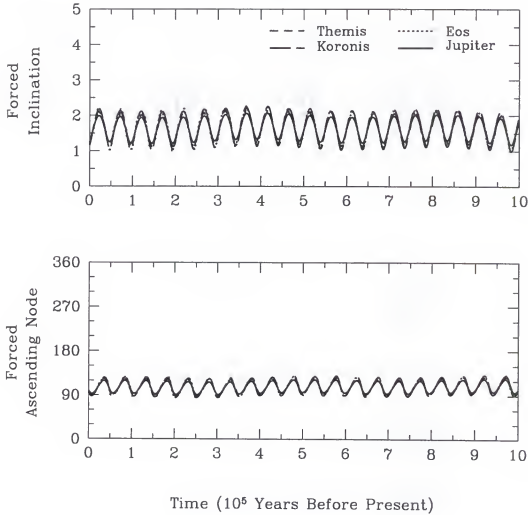


Figure 5-3: Comparison of the forced inclination and forced longitude of ascending node of the asteroid families Eos, Themis and Koronis with the inclination and longitude of ascending node of Jupiter's orbit. The orbital elements of the members of these three asteroid families were determined by backwards integration of the Solar System with the RADAU integrator (Mercury and Pluto excluded). These orbital elements are with respect to the J2000 ecliptic and mean equinox. The forced plane of symmetry of these three asteroid families is essentially locked onto the orbit of Jupiter.

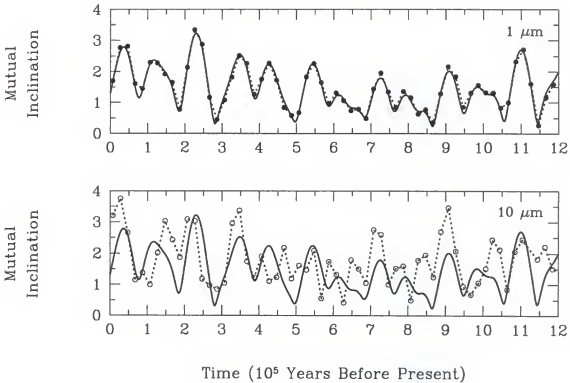


Figure 5-4: Waves of 249 particles with diameters of 1 and 10 microns were released from the asteroid family Eos every 20,000 years. These waves became Earth-crossing at the time indicated on the horizontal axis. At this point the mutual inclination between the orbit of the Earth and the forced plane of symmetry of each wave is calculated (1 micron – filled circle; 10 micron – open circle). The solid line is the mutual inclination between the orbits of the Earth and Jupiter from Quinn *et al.* Since the forced plane of symmetry of the asteroid families is locked onto the orbit of Jupiter (see Figure 5-3) this solid line represents the initial forced plane of symmetry of the waves of dust particles in the asteroid belt. This plot shows that the orbits of the 1 micron diameter particles decay into the inner Solar System so fast that they essentially retain their initial forced plane of symmetry. The 10 micron diameter particles evolve more slowly and therefore are more susceptible to perturbations which change their forced plane of symmetry.

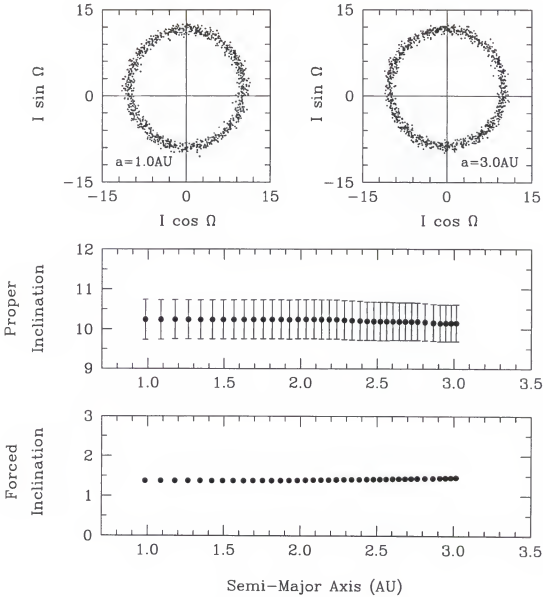


Figure 5-5: The orbital evolution of a wave of 1 micron diameter dust particles from the Eos family as their orbits decay from the asteroid family at 3AU into the inner Solar System. The middle plot tracks the evolution of the proper inclination and dispersion in proper inclination of the particles as their semi-major axes decay due to P-R drag. The displacement from the origin of the distributions in the upper two plots is due to the forced inclination, which is shown in the lower plot.

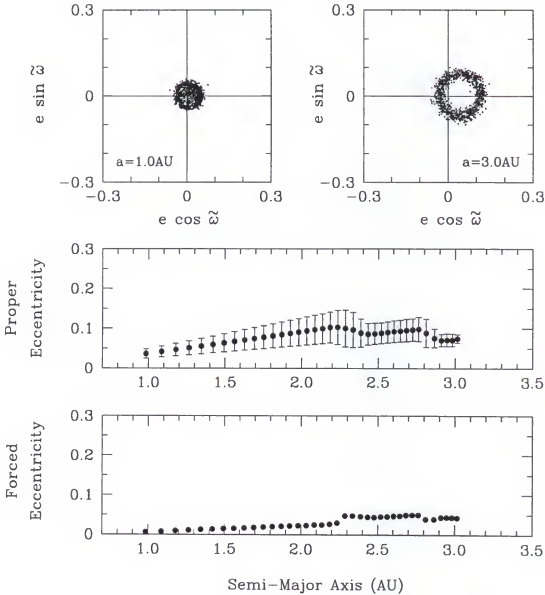


Figure 5-6: The orbital evolution of a wave of 1 micron diameter dust particles from the Eos family as their orbits decay from the asteroid family at 3AU into the inner Solar System. The middle plot tracks the evolution of the proper eccentricity and dispersion in proper eccentricity of the particles as their semi-major axes decay due to P-R drag. P-R drag also acts to reduce the proper eccentricity of the particles as their orbits decay towards the Sun. The displacement from the origin of the distributions in the upper two plots is due to the forced eccentricity, which is shown in the lower plot. At 1AU the distribution is nearly centered on the origin, indicating a very small forced eccentricity.

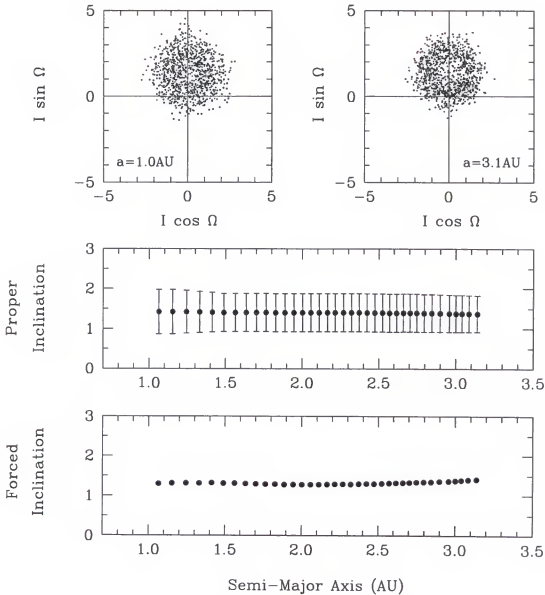


Figure 5-7: The orbital evolution of a wave of 1 micron diameter dust particles from the Themis family as their orbits decay from the asteroid family at 3.1 AU into the inner Solar System. The middle plot tracks the evolution of the proper inclination and dispersion in proper inclination of the particles as their semi-major axes decay due to P-R drag. The displacement from the origin of the distributions in the upper two plots is due to the forced inclination, which is shown in the lower plot.

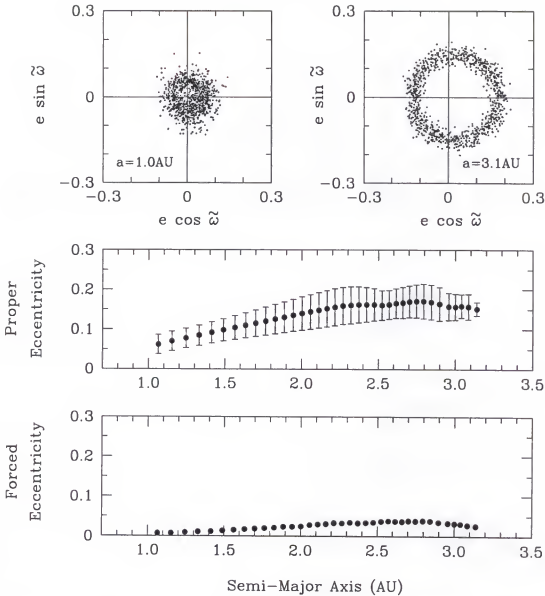


Figure 5-8: The orbital evolution of a wave of 1 micron diameter dust particles from the Themis family as their orbits decay from the asteroid family at 3.1 AU into the inner Solar System. The middle plot tracks the evolution of the proper eccentricity and dispersion in proper eccentricity of the particles as their semi-major axes decay due to P-R drag. P-R drag also acts to reduce the proper eccentricity of the particles as their orbits decay towards the Sun. The displacement from the origin of the distributions in the upper two plots is due to the forced eccentricity, which is shown in the lower plot. At 1AU the distribution is nearly centered on the origin, indicating a very small forced eccentricity.

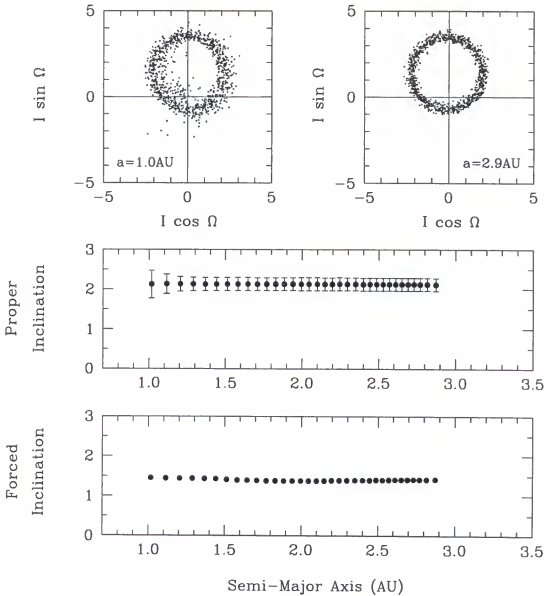


Figure 5-9: The orbital evolution of a wave of 1 micron diameter dust particles from the Koronis family as their orbits decay from the asteroid family at 2.9 AU into the inner Solar System. The middle plot tracks the evolution of the proper inclination and dispersion in proper inclination of the particles as their semi-major axes decay due to P-R drag. The displacement from the origin of the distributions in the upper two plots is due to the forced inclination, which is shown in the lower plot.

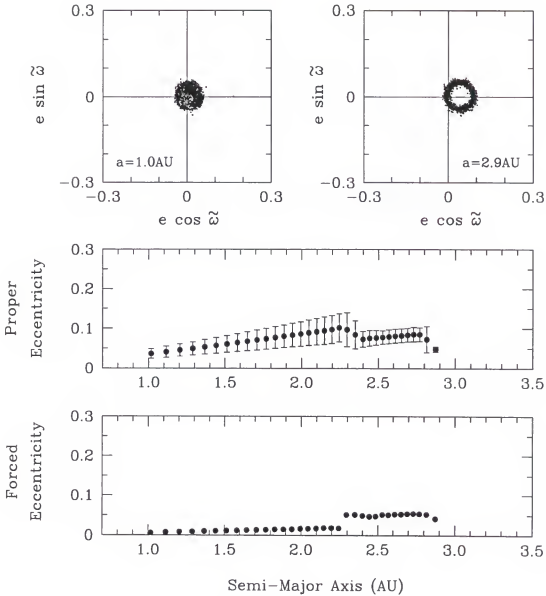


Figure 5-10: The orbital evolution of a wave of 1 micron diameter dust particles from the Koronis family as their orbits decay from the asteroid family at 2.9 AU into the inner Solar System. The middle plot tracks the evolution of the proper eccentricity and dispersion in proper eccentricity of the particles as their semi-major axes decay due to P-R drag. P-R drag also acts to reduce the proper eccentricity of the particles as their orbits decay towards the Sun. The displacement from the origin of the distributions in the upper two plots is due to the forced eccentricity, which is shown in the lower plot. At 1AU the distribution is nearly centered on the origin, indicating a very small forced eccentricity.

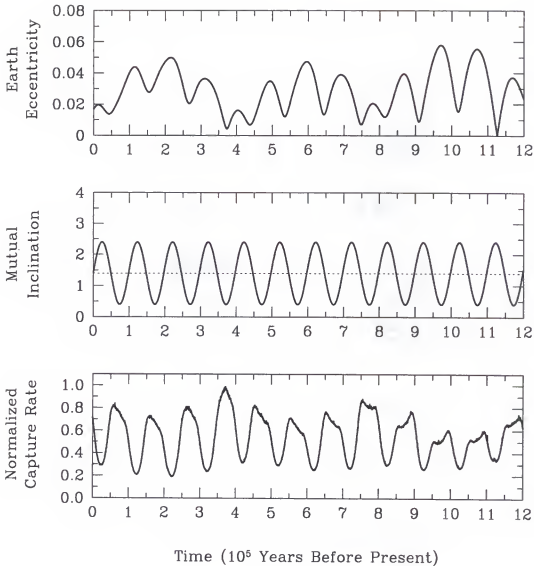


Figure 5-11: Demonstration of the variation in the capture rate: (Top) Varying eccentricity of the Earth's orbit from Quinn *et al.*; (Middle) Sine wave variation in the mutual inclination between the orbit of the Earth and the forced plane of symmetry of a dust band at 1AU. The base line of the mutual inclination is 1.°4; (Bottom) Variation in the normalized capture rate for dust particles with proper elements and dispersions equal to those of Themis 1 micron diameter particles at 1AU (See Table 5-1). The proper inclination is indicated by the dashed line in the middle plot. The variation of the Earth's eccentricity reveals itself in the capture rate, which appears to have been lopped off at points where the eccentricity is increasing or decreasing. There is also a subtle 400,000 periodicity in the varying capture rate due to the eccentricity, this is superimposed over the 100,000 year periodicity due to the mutual inclination.

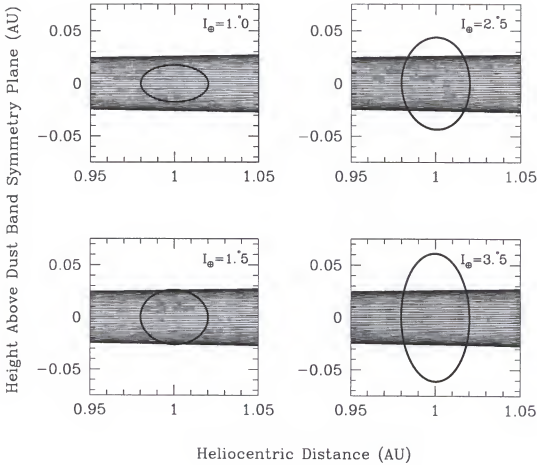


Figure 5-12: Demonstration of the annual motion of the Earth through an ideal dust band. The orbits in this idealized dust band have a proper inclination of 1.5° and no dispersion in proper inclination. Four different values of the mutual inclination (I_{\oplus}) between the orbit of the Earth and the forced plane of symmetry of the dust band are shown. When the mutual inclination is lower than the proper inclination of the dust band the Earth is embedded within the dust band throughout its entire orbit. However, when the mutual inclination is greater than the proper inclination of the dust band the Earth emerges from the dust band twice each year. The higher the mutual inclination is, the less time the Earth spends in the dust band each year. Also, the higher mutual inclination leads to greater geocentric encounter velocities of the dust particles when the Earth is in the dust band.

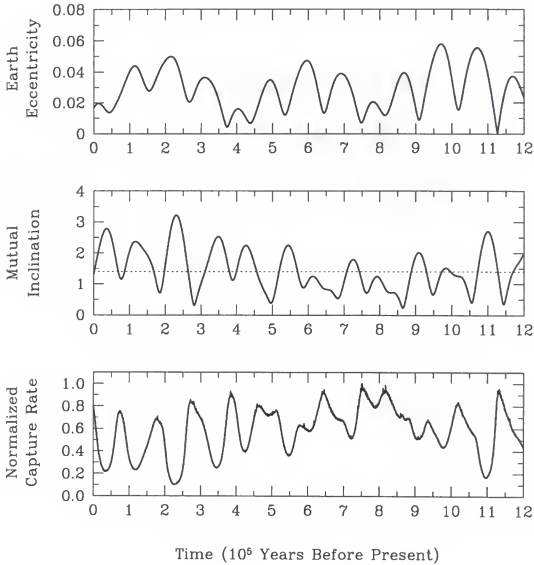


Figure 5-13: Variation in the capture rate of 1 micron diameter Themis particles: (Top) Varying eccentricity of the Earth's orbit from Quinn *et al.*; (Middle) Variation in the mutual inclination between the orbit of the Earth and the forced plane of symmetry of 1 micron diameter dust particles at 1AU; (Bottom) Variation in the normalized capture rate for dust particles with proper elements and dispersions equal to those of Themis 1 micron diameter particles at 1AU (See Table 5-1). The proper inclination is indicated by the dashed line in the middle plot. The capture rate of these small Themis dust particles drops dramatically when the Earth is not embedded within the dust band.

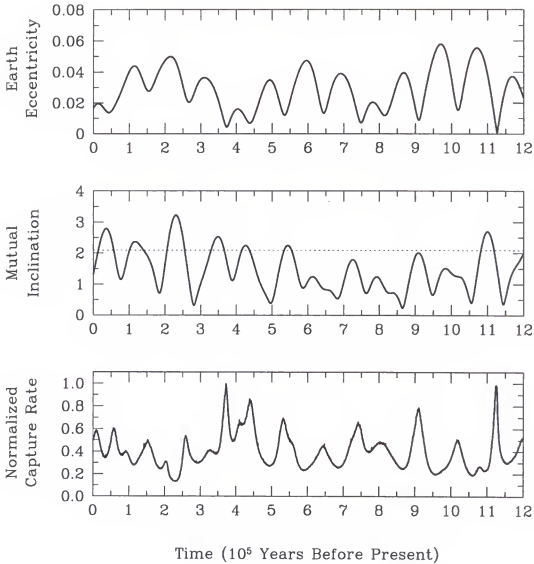


Figure 5-14: Variation in the capture rate of 1 micron diameter Koronis particles: (Top) Varying eccentricity of the Earth's orbit from Quinn *et al.*; (Middle) Variation in the mutual inclination between the orbit of the Earth and the forced plane of symmetry of 1 micron diameter dust particles at 1AU; (Bottom) Variation in the normalized capture rate for dust particles with proper elements and dispersions equal to those of Koronis 1 micron diameter particles at 1AU (See Table 5-1). The proper inclination is indicated by the dashed line in the middle plot. Because of the higher proper inclination the mutual inclination doesn't rise as far above the proper inclination and so the capture rate variations are not as dramatic as for the Themis particles.

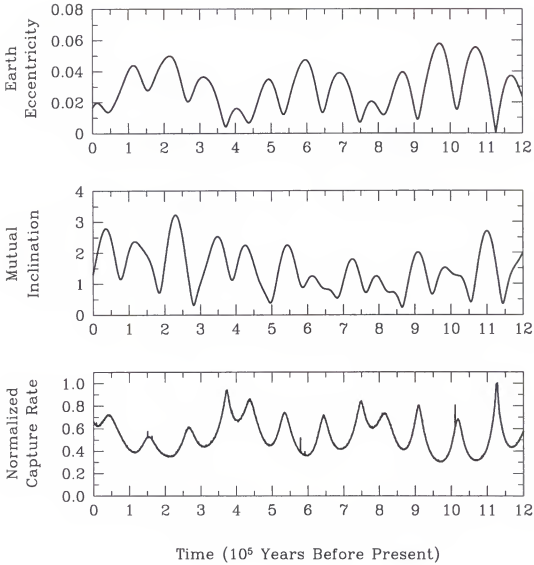


Figure 5-15: Variation in the capture rate of 1 micron diameter Eos particles: (Top) Varying eccentricity of the Earth's orbit from Quinn *et al.*; (Middle) Variation in the mutual inclination between the orbit of the Earth and the forced plane of symmetry of 1 micron diameter dust particles at 1 AU; (Bottom) Variation in the normalized capture rate for dust particles with proper elements and dispersions equal to those of Eos 1 micron diameter particles at 1 AU (See Table 5-1). Only the variation due to the Earth's eccentricity is evident in the capture rates.

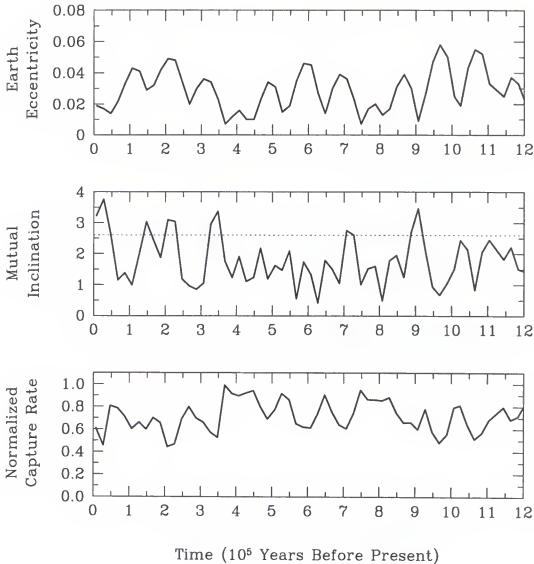


Figure 5-16: Variation in the capture rate of 10 micron diameter Themis and Koronis particles: (Top) Varying eccentricity of the Earth's orbit from Quinn *et al.*; (Middle) Variation in the mutual inclination between the orbit of the Earth and the forced plane of symmetry of 10 micron diameter dust particles at 1AU; (Bottom) Variation in the normalized capture rate for dust particles with proper elements and dispersions equal to those of Themis and Koronis 10 micron diameter particles at 1AU (See Table 5-2). The proper inclination is indicated by the dashed line in the middle plot. Because of the higher proper inclination and the higher dispersion the capture rates of these larger particles do not show the large variations associated with the smaller 1 micron diameter particles.

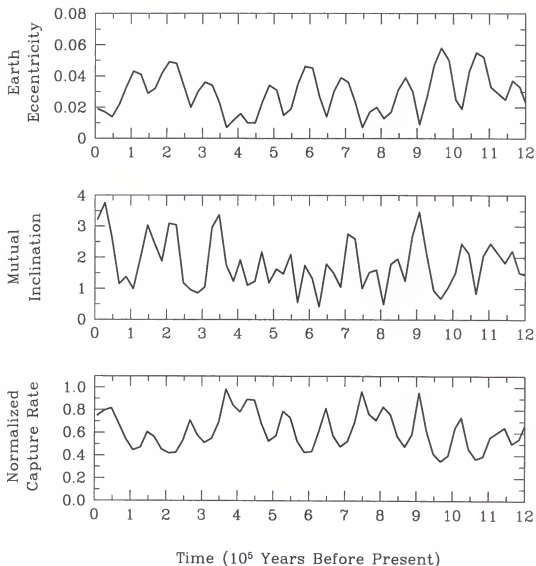


Figure 5-17: Variation in the capture rate of 10 micron diameter Eos particles: (Top) Varying eccentricity of the Earth's orbit from Quinn *et al.*; (Middle) Variation in the mutual inclination between the orbit of the Earth and the forced plane of symmetry of 10 micron diameter dust particles at 1AU; (Bottom) Variation in the normalized capture rate for dust particles with proper elements and dispersions equal to those of Eos 10 micron diameter particles at 1AU (See Table 5-2). The effect of the varying mutual inclination is completely absent from the capture rate and only the variation due to the Earth's eccentricity remains. Since Eos particles have a proper inclination about equal to the mean for the asteroid belt we expect that any variation in the accretion of background asteroidal particles will follow the variations shown here.

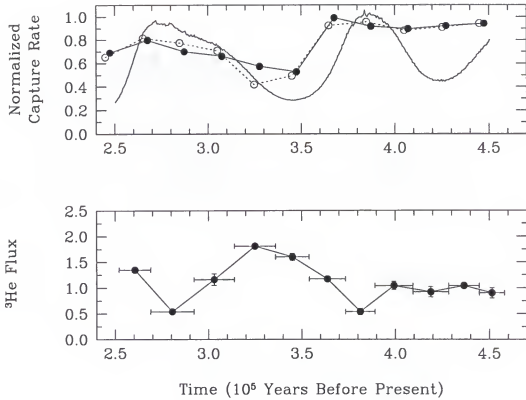


Figure 5-18: Comparison of the capture rates for Themis and Koronis particles with the ^3He record for the period between 250,000 and 450,000 years ago: (Top) Capture rates (Gyr^{-1}) for particles of diameter 20 (open circles), 10 (solid circles) and 1 micron (high resolution line – Themis only); (Bottom) Variation in the flux of extraterrestrial ^3He ($10^{-12} \text{ cm}^3 \text{ STP cm}^{-2} \text{ kyr}^{-1}$) to the sea floor from Farley and Patterson (1995). Only the 1 micron diameter capture rate displays a variation with an amplitude and period comparable with that of the ^3He flux, however, the two curves are not in phase.

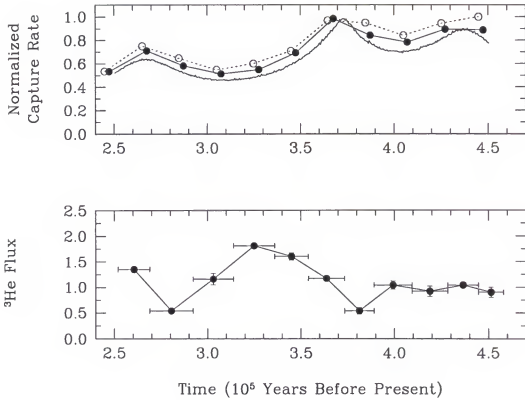


Figure 5-19: Comparison of the capture rates for Eos particles with the ^3He record for the period between 250,000 and 450,000 years ago: (Top) Capture rates (Gyr^{-1}) for particles of diameter 20 (open circles), 10 (solid circles) and 1 micron (high resolution line); (Bottom) Variation in the flux of extraterrestrial ^3He ($10^{-12} \text{ cm}^3 \text{ STP cm}^{-2} \text{ kyr}^{-1}$) to the sea floor from Farley and Patterson (1995). Note that only the 1 micron diameter capture rate displays a variation with an amplitude and period comparable with that of the ^3He flux, however, the two curves are not in phase.

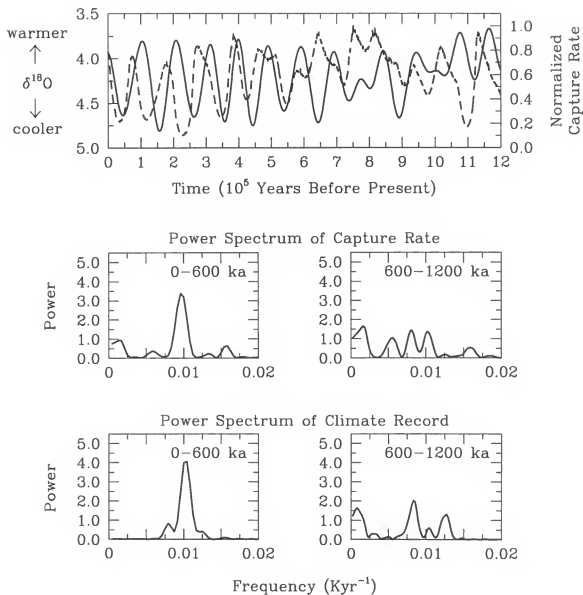


Figure 5-20: Comparison of the capture rates for 1 micron diameter Themis particles with the climate record for the last 1.2 million years: (Top) Normalized capture rate for 1 micron diameter Themis particles (dashed line) and the filtered climate record (solid line, $\delta^{18}\text{O}$ – oxygen isotope ratios in deep-sea sediments) for the last 1.2 million years. The climate record is shown after removal of the well understood shorter period Milankovitch frequencies (Imbrie *et al.* 1993); (Middle) Power spectrum of the capture rate for 0–600 ka (ka – 10^3 years ago) and 600–1200 ka; (Bottom) Power spectrum of filtered climate record for 0–600 ka and 600–1200 ka.

CHAPTER 6

SUMMARY

Conclusions and Discussion

Asteroids and comets are the best available examples of the building blocks from which the planets in the Solar System formed. Interplanetary dust particles collected from the Earth's atmosphere are derived from asteroids and comets and, together with the meteorites, are the only primitive materials available for laboratory analysis. It is important to identify the sources of these samples and to understand how they dynamically evolve from their source regions and subsequently accumulate on the surface of the Earth.

Our work builds upon the foundation of the IRAS observations of the zodiacal cloud. Following a logical sequence of events we argue that most of the interplanetary dust particles accreted by the Earth probably originate in the asteroid belt and that a large and perhaps dominant fraction of this dust comes from just three asteroid families – Eos, Themis and Koronis. Speculating on the importance of this, we point out that at the current rate of accretion ($3 \times 10^7 \text{ kg yr}^{-1}$) the Earth would have accumulated about 10^{17} kg of asteroidal dust since its formation. Furthermore, studies of the collisional evolution of the asteroid belt indicate that the primordial belt may have been a factor of 10^3 more massive than the current belt (Durda and Dermott 1996), thereby possibly increasing the total mass of accreted dust to near 10^{20} kg . If the average density of this asteroidal material is about 2 g cm^{-3} then these two estimates result in the equivalent of a layer of asteroidal dust covering the surface of the Earth to a depth between 0.1 and 100 meters. Thus, the transport of carbonaceous material from the asteroid belt to

the inner Solar System and its gentle deposition in the Earth's atmosphere could offer a means of supplying organic material to the Earth without dissociation, after the surface of the planet had cooled and solidified.

We have also shown that changes in the orbital elements of the Earth may lead to significant periodic variations in the accretion rate of dust from the Eos, Themis and Koronis families. There is also some evidence for variations in the accretion rate over much longer time scales. Farley (1995) has measured the extraterrestrial ^3He in a deep-sea sediment core sample dating back nearly 70 million years and has found evidence for significant non-periodic variations in the influx of interplanetary dust lasting millions of years. Farley suggests that these variations could be due to the breakup of asteroids. Durda *et al.* (1992) modeled the dust production rate associated with the creation and evolution of an asteroid family beginning with the catastrophic disruption of a 300km asteroid, shown in Figure 6-1. The stochastic spiky nature of Figure 6-1, especially after several billion years of evolution, is due to the continuing breakup of smaller 10-40 km bodies in the family which produce huge surges of dust, increasing the amount of dust associated with the family by as much as 10^3 . These surges last for tens of million years and would have enshrouded the Earth in a dust band perhaps a thousand times more dense the bands we have today. This could have increased the annual influx of dust particles to the mega ton range. This amount of dust is comparable with the output due to large volcanic eruptions and would have caused serious changes in the Earth's climate for many millions of years. Disruption of these large asteroids might also deposit large asteroidal fragments into chaotic regions of resonance in the asteroid belt, where some of them would be subsequently perturbed into Earth-crossing orbits. The time scale for these perturbations is also in the millions of years. During these times the Earth would be enshrouded in a dense asteroidal dust band and at the same time would be at an

increased risk of impact from a fresh supply of Earth-crossing asteroids. A combination of these two events could result in several drawn out extinction events lasting tens of millions of years, some of which (though possible not all) might be punctuated by single or multiple impacts events.

Future Work – The Role of Resonance

Analysis of micrometeorite craters on the space facing panels of LDEF resulted in an estimate of the total annual mass influx of $3 \times 10^7 \text{ kg yr}^{-1}$ (Love and Brownlee 1993). Craters corresponding to dust particle diameters between 5 and 500 micron were counted and an incremental mass influx for particles in this range was determined. Figure 6-2 shows the incremental mass influx per log mass interval in this size range. Most of the mass is contained in the larger particles and there is a particle-size cutoff near 200 micron diameter. When a plot is made showing the cross-sectional area influx (Figure 6-3) we see that here also the larger particles are contributing more than the smaller ones. This is contrary to conventional wisdom which suggests that most of the area in a population of collisionally evolved bodies should be in the smallest particles. Does the LDEF cratering record suggest a paucity of small particles or an over abundance of large particles? Either way, this may be taken as evidence that we should be investigating the dynamics of particles much larger than those that we have analyzed to date.

The literature dealing with orbital interactions and accretion includes four frequently cited papers – Öpik (1951), Wetherill (1967), Kessler (1981) and Greenberg (1982). One of the primary assumptions made in each of these papers is that the two interacting bodies being studied are not in resonance with each other. This assumption also applies to our work. Without resonant trapping most dust particles spiral past the Earth, failing to strike the planet due to their extremely low capture rates. (The rates are in inverse *billion* years

after all.) However, we know that 20% to 30% of the asteroidal dust particles larger than 5 microns diameter become trapped in the Earth's resonant ring for some length of time (Dermott *et al.* 1994). These resonances create a bottle neck of sorts for large asteroidal particles in the vicinity of the Earth. We have briefly investigated the behavior of these trapped particles.

Figures 6-4 and 6-5 track the orbital evolution of two 20 micron diameter particles that become trapped in resonance. While the particles are in resonance, forces act to maintain their semi-major axes and initially to prevent them from encountering the Earth. The cost of this initial isolation is an increase in the orbital eccentricity associated with the particle. Coupled with the near constant semi-major axis the rising eccentricity will eventually result in the perihelion of the particle falling inside of 1 AU, at which point the orbit becomes Earth-crossing by definition. The growing eccentricity and attainment of Earth-crossing status eventually may result in an encounter with the Earth and the subsequent release of the particle from resonance, as appears to have happened for the two particles in Figures 6-4 and 6-5. It is precisely this sequence of events which leads us to believe that particles trapped in the ring may be preferentially captured by the Earth over untrapped particles. If this is true the ring could have important implications on the efficiency of the transport of carbonaceous material from the asteroid belt to the Earth. It will also mean that the size frequency distribution of particles captured by the Earth directly from resonance will be quite different from that of particles that strike the Earth without resonance trapping. This could help explain the cratering record on LDEF shown in Figures 6-2 and 6-3. Changes in the Earth's orbital eccentricity could result in variations in the density of the ring and in accretion of particles from the ring, which may account for the $^3\text{He}/^{230}\text{Th}$ findings of Marcantonio *et al.* (1996) and possibly shed light on the climate problem.

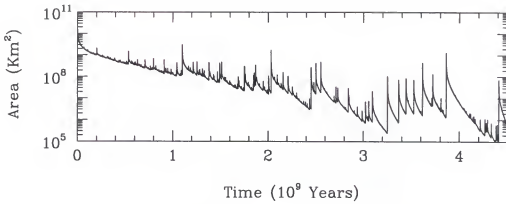


Figure 6-1: Stochastic variations in the cross-sectional area of debris down to 1mm from the breakup of a large asteroid and its continued collisional evolution. The area associated with the fragments is an indicator of the dust production rate of the debris. The smaller spikes are due to the continuing breakup of smaller 10–40 km diameter bodies. This figure is from Durda *et al.* (1992).

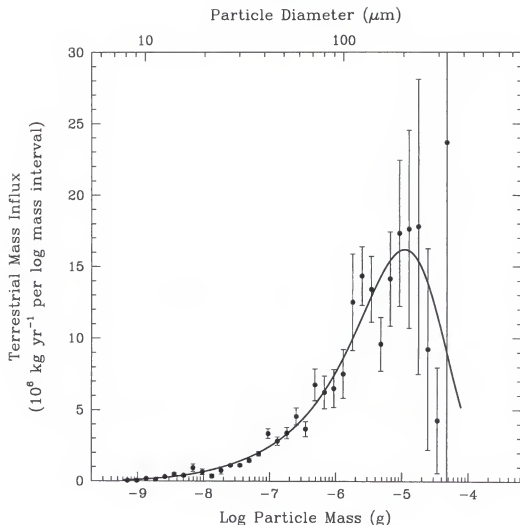


Figure 6-2: Incremental mass of particles accreted by the Earth annually as a function of particle mass and diameter (number in each bin times the average mass for each bin). The bold line is calculated from the polynomial derived by Love and Brownlee (1993) from the cratering record on LDEF. The individual points with errors are calculated from the incremental crater density counts provided by S. Love (personal communication). As expected, the mass accretion is dominated by the larger particles.

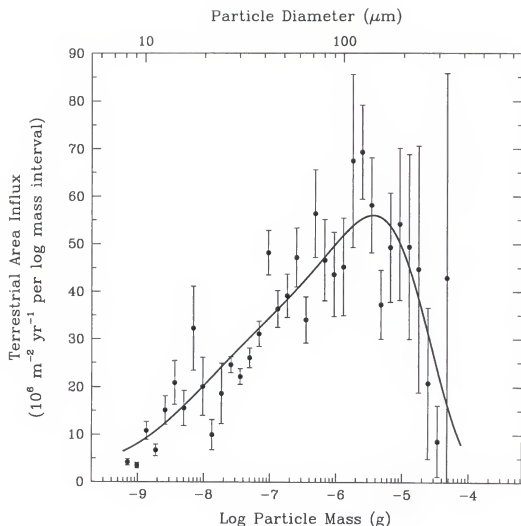


Figure 6-3: Incremental cross-sectional area of particles accreted by the Earth annually as a function of particle mass and diameter (number in each bin times the average cross-section for each bin). Note that the area in the larger particle bins dominates that of the smaller particles, contrary to the long held notion that smaller particles contribute more area than larger particles. One way of interpreting this is that there is an over abundance of larger particles being accreted by the Earth. Also note that there is a cutoff near a particle diameter of 150 μm .

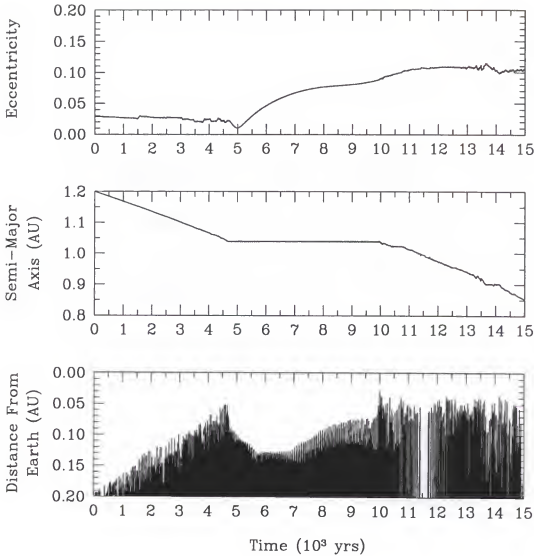


Figure 6-4: The orbital evolution of a $20\mu\text{m}$ diameter dust particle. From left to right we see the semi-major axis (middle) of the particle orbit decay until it becomes trapped in a first order outer mean-motion resonance with the Earth after about 4500 years. At this point the semi-major axis remains roughly constant while the eccentricity (top) begins to increase. While the orbit is decaying the distance of the particle from the Earth (bottom) decreases. Then, upon capture the particle is initially kept away from the Earth by the resonance. As the eccentricity increases the gap between the Earth and particle narrows until eventually the particle is released from the resonance after being trapped for about 5000 years.

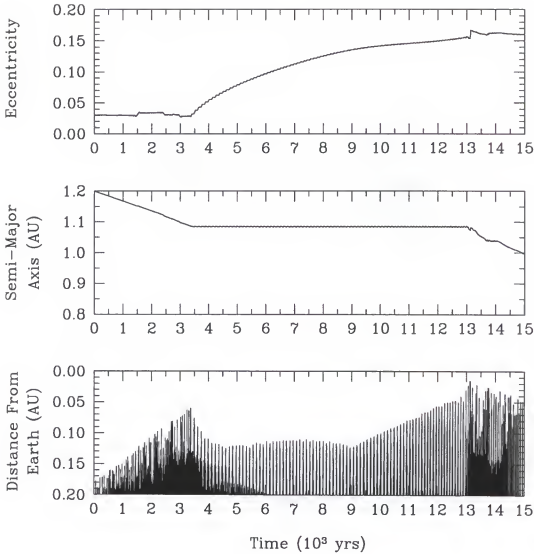


Figure 6-5: Evolution of another $20\mu\text{m}$ diameter dust particle which remains trapped in resonance for nearly 10,000 years. Note once again that while in resonance the particle is initially prevented from having a close encounter with the Earth (bottom). However, as the eccentricity (top) increases the particle is brought nearer and nearer until eventually experiencing a close encounter with the Earth and being released from the resonance.

BIBLIOGRAPHY

- Binzel, R.P., T. Gehrels and M. Matthews (Eds.) 1988. *Asteroids II*. University of Arizona Press, Tuscon.
- Binzel, R.P. and S. Xu 1993. Chips off of asteroid 4 Vesta: Evidence for the parent body of basaltic achondrite meteorites. *Science* **260**, 186–191.
- Brownlee, D.E. 1978. Microparticle studies by sampling techniques. In *Cosmic Dust* (J.A.M. McDonnell, Ed.), pp. 275–336. Wiley, Chichester.
- Brownlee, D.E. 1995. Interplanetary dust: A driver of glaciation cycles? *Nature* **378**, 558.
- Dermott, S.F., P.D. Nicholson, J.A. Burns and J.R. Houck 1984. Origin of the Solar System dust bands discovered by IRAS. *Nature* **312**, 505–509.
- Dermott, S.F., R.S. Gomes., D.D. Durda, B.Å.S. Gustafson, S. Jayaraman, Y.L. Xu and P.D. Nicholson 1992a. Dynamics of the zodiacal cloud. In *Chaos, Resonance, and Collective Dynamical Phenomena in the Solar System* (S. Ferraz-Mello, Ed.), pp. 333–347, Kluwer, Dordrecht.
- Dermott, S.F., D.D. Durda, B.Å.S. Gustafson, S. Jayaraman, Y.L. Xu, R.S. Gomes and P.D. Nicholson 1992b. The origin and evolution of the zodiacal dust cloud. In *Asteroids, Comets & Meteors 1991* (A.W. Harris and E. Bowell, Eds.), pp. 153–156, Lunar and Planetary Institute, Houston.
- Dermott, S.F., D.D. Durda, R.S. Gomes, B.Å.S. Gustafson, S. Jayaraman, J.C. Liou, P.D. Nicholson and Y.L. Xu 1993. The origin of the IRAS dust bands. In *Meteoroids and Their Parent Bodies* (J. Stohl and I.P. Williams Eds.), pp. 357–366, Astronomical Inst., Slovak. Acad. Sci., Bratislava.
- Dermott, S.F., D.D. Durda, B.Å.S. Gustafson, S. Jayaraman, J.C. Liou and Y.L. Xu 1994a. Zodiacal dust bands. In *Asteroids, Comets, Meteors 1993* (A. Milani, M. Martini and A. Cellino, Eds.), pp. 127–142, Kluwer, Dordrecht.
- Dermott, S.F., S. Jayaraman, Y.L. Xu, B.Å.S. Gustafson, and J.C. Liou 1994b. A circumsolar ring of asteroidal dust in resonant lock with the Earth. *Nature* **369**, 719–723.
- Durda, D.D., S.F. Dermott and B.Å.S. Gustafson 1992. Modeling of asteroidal dust production rates. In *Asteroids, Comets & Meteors 1991* (A.W. Harris and E. Bowell, Eds.), pp. 161–164, Lunar and Planetary Institute, Houston.
- Durda, D.D. and S.F. Dermott 1996. The collisional evolution of the asteroid belt and its contribution to the zodiacal cloud. *Icarus* (in press).

- Draine, B.T. and H.M. Lee 1984. Optical properties of interstellar graphite and silicate grains. *Astrophys. J.* **285**, 89–108.
- Everhart, E. 1985. In *Dynamics of Comets* (A. Carusi and G.B. Valsecchi, Eds.) pp. 185–202, Reidel, Dordrecht.
- Farley, K.A. 1995. Cenozoic variations in the flux of interplanetary dust recorded by ^3He in a deep-sea sediment. *Nature* **376**, 153–156.
- Farley, K.A. and D.B. Patterson 1995. A 100-kyr periodicity in the flux of extraterrestrial ^3He to the sea floor. *Nature* **378**, 600–603.
- Farley, K.A., S.G. Love and D.B. Patterson 1996. Atmospheric entry heating and helium retentivity of interplanetary dust particles. *Geochim. Cosmochim. Acta*. (submitted).
- Flynn, G.J. 1990. The near-Earth enhancement of asteroidal over cometary dust. In *Proc. 20th Lunar and Plan. Sci. Conf.* pp. 363–371, Lunar and Planetary Institute, Houston.
- Flynn, G.J. 1994. Changes in the zodiacal cloud. *Nature* **376**, 114.
- Greenberg, R. 1982. Orbital interactions: A new geometrical formalism. *Astron. J.* **87** (1), 184–195.
- Grogan, K., S.F. Dermott, S. Jayaraman, and Y.L. Xu 1996. Origin of the ten degree Solar System dust bands. *Planet. Space Sci.* (submitted).
- Grün, E. 1994. Dust measurements in the outer Solar System. In *Asteroids, Comets, Meteors 1993* (A. Milani, M. Martini and A. Cellino, Eds.), pp. 367–380, Kluwer, Dordrecht.
- Grün, E., H.A. Zook, H. Fechtig and R.H. Giese 1985. Collisional balance of the meteoritic complex. *Icarus* **62**, 244–272.
- Gustafson, B.Å.S. 1994. Physics of zodiacal dust. *Ann. Rev. Earth Planet Sci.* **22**, 553–595.
- Gustafson, B.Å.S., E. Grün, S.F. Dermott and D.D. Durda 1992. Collisional and dynamic evolution of dust from the asteroid belt. In *Asteroids, Comets & Meteors 1991*, (A.W. Harris and E. Bowell, Eds.), pp. 223–226, Lunar and Planetary Institute, Houston.
- Imbrie, J., A. Berger, E.A. Boyle, S.C. Clements, A. Duffy, W.R. Howard, G. Kukla, J. Kutzbach, D.G. Martinson, A. McIntyre, A.C. Mix, B. Molino, J.J. Morley, L.C. Peterson, N.G. Pisias, W.L. Prell, M.E. Raymo, N.J. Shackleton and J.R. Toggwiler 1993. On the structure and origin of major glaciation cycles 2: The 100,000 year cycle. *Paleoceanography* **8**, 699–735.

- Jayaraman, S. and S.F. Dermott 1995. COBE/DIRBE observations of the Earth's resonant ring. In *Unveiling the Cosmic Infrared Background*, (E. Dwek, Ed.), pp. 47–52, AIP Press.
- Kerr, R.A. 1996. New source proposed for most common meteorites. *Science* **273**, 1337.
- Kerridge, J.F. and M.S. Mathews (Eds.) 1988. *Meteorites and the Early Solar System*. University of Arizona Press, Tucson.
- Kessler, D.J. 1981. Derivation of the collision probability between orbiting objects: The lifetime of Jupiter's outer moons. *Icarus* **48**, 39–48.
- Kortenkamp, S.J., S.F. Dermott and J.C. Liou 1996. Naturally occurring selection effects on the terrestrial accretion of interplanetary dust particles. In *Physics, Chemistry and Dynamics of Interplanetary Dust, ASP Conf. Series 104* (B.Å.S. Gustafson and M.S. Hanner, Eds.), pp. 167–170, ASP Publications, San Francisco.
- Kortenkamp, S.J., S.F. Dermott and K. Grogan 1996. Asteroid families dominate comets as sources of extraterrestrial dust accreted by the Earth. *Nature* (submitted).
- Leinert, C. and E. Grün 1990. Interplanetary dust. In *Physics and Chemistry in Space – Space and Solar Physics, Vol. 20 Physics of the Inner Heliosphere I* (R. Schwenn and E. Marsch, Eds.), pp. 207–275, Springer-Verlag, Berlin.
- Liou, J.C. and S.F. Dermott 1995. The contribution of cometary dust to the zodiacal cloud. *Planet. Space Sci.* **43–6**, 717–722.
- Liou, J. C., H. Zook and S.F. Dermott 1995. Orbital evolution of micron-sized dust grains coming from the Kuiper belt. In *Proc. Lunar and Plan. Sci. Conf.*
- Lipschutz, M.E., M.J. Gaffey and P. Pellas 1989. In *Asteroids II* (R. Binzel, T. Gehrels and M. Matthews, Eds.), pp. 740–777, University of Arizona Press, Tucson.
- Love, S.G. and D.E. Brownlee 1992. The IRAS dust band contribution to the interplanetary dust complex: Evidence seen at 60 and 100 microns. *Astrophys. J.* **104** (6), 2236–2242.
- Love, S.G. and D.E. Brownlee 1993. A direct measurement of the terrestrial mass accretion rate of cosmic dust. *Science* **262**, 550–553.
- Low, F.L. 1984. Infrared cirrus: New components of the extended infrared emission. *Astrophys. J. Letters* **278**, L19–L22.
- McKay, D.S., E.K. Gibson Jr., K.L. Thomas-Keprta, H. Vali, C.S. Romanek, S.J. Clement, X.D.F. Chillier, C.R. Maechling and R.N. Zare 1996. Search for past life on Mars: Possible relic biogenic activity in martian meteorite ALH84001. *Science* **273**, 924–930.

- Marcantonio, F., R.F. Anderson, M.S. Stute, N. Kumar, P. Schlosser and A. Mix 1996. Extraterrestrial ^3He as a tracer of marine sediment transport and accumulation. *Nature* **383**, 705–707.
- Muller, R.A. and G.J. MacDonald 1995. Glacial cycles and orbital inclination. *Nature* **377**, 107–108.
- Öpik, E.J. 1951. Collision probabilities with the planets and the distribution of interplanetary matter. *Proc. Royal Irish Academy* **54-A**, 165–199.
- Quinn, T.R., S. Tremaine and M. Duncan 1991. A three million year integration of the Earth's orbit. *Astron. J.* **101**, 2287–2305.
- Reach, W.T., B.A. Franz, J.L. Weiland, M. Hauser, T.N. Kelsall, E.L. Wright, G. Rawley, S.W. Stemwede and W.J. Spiesman 1995. Observational confirmation of a circumsolar dust ring by the COBE satellite. *Nature* **374**, 521–523.
- Sykes, M.V., R.J. Greenberg, S.F. Dermott, P.D. Nicholson, J.A. Burns and T.N. Gautier, III 1989. Dust bands in the asteroid belt. In *Asteroids II* (R. Binzel, T. Gehrels and M. Matthews, Eds.), pp. 336–367, University of Arizona Press, Tucson.
- Wetherill, G.W. 1967. Collisions in the asteroid belt. *J. Geophys. Res.* **72** (9), 2429–2444.
- Wetherill, G.W. 1988. Where do the Apollo objects come from? *Icarus* **76**, 1–18.
- Wetherill, G.W. and L.P. Cox 1985. The range of validity of the two-body approximation in models of terrestrial planet accumulation II: Gravitational cross-sections and runaway accretion. *Icarus* **63**, 290–303.
- Wetherill, G.W. and C.R. Chapman 1988. Asteroids and meteorites. In *Meteorites and the Early Solar System* (J.F. Kerridge and M.S. Mathews, Eds.), pp. 35–67, University of Arizona Press, Tucson.
- Whipple, F.L. 1967. On maintaining the meteoritic complex. *Smithsonian Astrophysical Observatory Special Report* **239**, 1–46.
- Wisdom, J. 1985. Meteorites may follow a chaotic route to Earth. *Nature* **315**, 731–733.

BIOGRAPHICAL SKETCH

Stephen John Kortenkamp was born in 1968 and raised in Stevens Point, Wisconsin along the banks of the Wisconsin River, a tributary to the mighty Mississippi. In 1990 he earned his undergraduate degrees in physics and mathematics from the University of Wisconsin at Eau Claire, the campus of which straddles the Eau Claire River, another tributary to the mighty Mississippi. In 1992 he moved to Gainesville, Florida, through which no river runs.

Stephen is the third oldest in a family of nine children. His will be the fourth doctorate in the family behind his father Daniel (Ph.D. – University of Iowa), older brother David (Ph.D. – University of Michigan) and older sister Suzanne (J.D. – University of Wisconsin).

I certify that I have read this study and that in my opinion it conforms to acceptable standards of scholarly presentation and is fully adequate, in scope and quality, as a dissertation for the degree of Doctor of Philosophy.



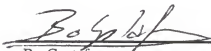
Stanley Dermott, Chair
Professor of Astronomy

I certify that I have read this study and that in my opinion it conforms to acceptable standards of scholarly presentation and is fully adequate, in scope and quality, as a dissertation for the degree of Doctor of Philosophy.



Humberto Campins
Associate Professor of Astronomy

I certify that I have read this study and that in my opinion it conforms to acceptable standards of scholarly presentation and is fully adequate, in scope and quality, as a dissertation for the degree of Doctor of Philosophy.



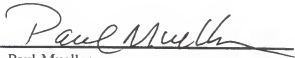
Bo Gustafson
Associate Professor of Astronomy

I certify that I have read this study and that in my opinion it conforms to acceptable standards of scholarly presentation and is fully adequate, in scope and quality, as a dissertation for the degree of Doctor of Philosophy.



Henry E. Kandrups
Associate Professor of Astronomy

I certify that I have read this study and that in my opinion it conforms to acceptable standards of scholarly presentation and is fully adequate, in scope and quality, as a dissertation for the degree of Doctor of Philosophy.



Paul Mueller
Professor of Geology

This dissertation was submitted to the Graduate Faculty of the Department of Astronomy in the College of Liberal Arts and Sciences, and to the Graduate School and was accepted as partial fulfillment of the requirements for the degree of Doctor of Philosophy.

December 1996

Dean, Graduate School